

See discussions, stats, and author profiles for this publication at: <https://www.researchgate.net/publication/24196049>

# Metal Speciation Dynamics in Soft Colloidal Ligand Suspensions. Electrostatic and Site Distribution Aspects

ARTICLE *in* THE JOURNAL OF PHYSICAL CHEMISTRY A · APRIL 2009

Impact Factor: 2.69 · DOI: 10.1021/jp809764h · Source: PubMed

---

CITATIONS

15

---

READS

26

## 1 AUTHOR:



[Jerome F.L. Duval](#)

French National Centre for Scientific Resea...

111 PUBLICATIONS 1,922 CITATIONS

SEE PROFILE

# Metal Speciation Dynamics in Soft Colloidal Ligand Suspensions. Electrostatic and Site Distribution Aspects

Jérôme F. L. Duval

Laboratory Environment and Mineral Processing, CNRS, Nancy-University, UMR 7569, BP 40 - F-54501 Vandoeuvre-lès-Nancy Cedex, France

Received: November 5, 2008; Revised Manuscript Received: December 17, 2008

The theory for metal speciation dynamics in dilute, monodisperse suspensions of spherical core–shell colloidal ligand particles is extended with the impact of the electric double layer (EDL) field and inhomogeneous site distribution inside the particle. The latter is defined by a diffuse, radial distribution for the density of charged polymer segments supporting the ligands L. The site distribution at the scale of the particle suspension and within the colloidal shell results in association/dissociation rate constants (denoted as  $k_a^*$  and  $k_d^*$ , respectively) that may significantly differ from their homogeneous solution counterparts ( $k_a$  and  $k_d$ ). The differences arise from intertwined kinetics of metal–ligand (ML) complex formation/dissociation in the particle shell and diffusive transport of free metal ions M within/outside the shell in the electric field set up by the EDL at the core–shell/electrolyte interphase. The relationship between  $k_{a,d}^*$  and  $k_{a,d}$  is derived from the numerical evaluation of the spatial, time-dependent distributions of free and bound metal as governed by coupled Nernst–Planck equations corrected by appropriate chemical source term and written in a Kuwabara cell geometry. The average interphasial electrostatic field stemming from the formation of the EDL at the complexing colloidal interphase is obtained from the solution of the nonlinear Poisson–Boltzmann equation. The EDL composition is exclusively governed by ions from indifferent background electrolyte present in large excess over free metal species M. The dependences of  $k_{a,d}^*$  on rate constants  $k_{a,d}$ , geometrical details of particle, particle charge, concentration of indifferent background electrolyte, and ligand distribution within the shell are thoroughly discussed within the context of dynamic features for colloidal complex systems. Examination of the chemical equilibrium regime allows addressing explicitly the impact of electrostatics on colloidal complex stability (polyelectrolyte effect). The numerical study is further supported by an approximate analytical expression based on Donnan partitioning and valid under the quasi-steady-state approximation (nonequilibrium chemical regime). The analysis covers the limiting cases of charged rigid particles where binding sites are located at the very surface of the core (e.g., functionalized latex colloids) and polyelectrolyte particles devoid of a hard core (e.g., polysaccharide macromolecules, gel particles).

## 1. Introduction

It is now well established that the quantitative understanding of metal speciation in aquatic media is a mandatory prerequisite for appropriately addressing the relationships between the various physicochemical forms of the metal species and their respective activity, mobility, or bioavailability.<sup>1</sup> Under environmental conditions, metal ions are typically distributed over a broad range of complexes that differ in size, geometry, and nature (mineral or organic).<sup>1,2</sup> This in turn gives rise to a formidable panel of metal complex properties in terms of lability and stability. Because natural aquatic media are never at equilibrium,<sup>1</sup> accurate conceptual frameworks are required to capture the basic dynamic aspects underlying the interconversion of metal complexes in bulk solution and at a given consuming interface, e.g., an electrode<sup>2–6</sup> or a microorganism.<sup>2,7,8</sup> Tackling adequately these aspects unavoidably necessitates invoking 3D kinetics of metal complex association/dissociation in conjunction with the various transport phenomena associated with the selective consumption/affinity, usually that of free metal ions, at/for a given interface.<sup>1,6–11</sup>

Until recently, dynamic theories disregarded the colloidal nature of metal complexes as originating from the interaction between metal ions and, e.g., humics, living organisms (bacteria), or polyelectrolyte particles such as polysaccharides.

Ligand distribution was instead considered as homogeneous throughout the solution volume<sup>10–13</sup> and the metal complex association/dissociation rate constants taken identical to those for their homogeneous solution counterparts. Such an assimilation intrinsically comes to ignore the very spatial confinement of ligands within the particle geometry. Pinheiro et al. quantitatively showed that this oversimplification may lead to an overestimation of the effective kinetic rate constants by several orders of magnitude with, as a consequence, dramatic misinterpretation of the metal complex dynamics and lability properties.<sup>6,14–16</sup> In more detail, their analysis demonstrated that the fundamental difference between metal speciation dynamics in homogeneous ligand solutions and colloidal ligand dispersions is due to the evolution from a chemically controlled release of the metal to a diffusion-controlled one. Their theory is valid under quasi-steady-state approximation and is applicable for hard colloidal particles with ligands distributed at the very particle surface. More recently, Duval et al.<sup>17</sup> formulated a comprehensive theory for metal speciation dynamics in suspensions of soft colloidal particles where binding sites are distributed according to three-dimensional spatial profiles. As argued previously,<sup>17</sup> such particles, which consist of a hard core surrounded by an ion-permeable shell layer, generally better describe particles of environmental relevancy such as humics, bacteria, or mineral

particles covered by adsorbed organic layers.<sup>18–24</sup> The treatment reported previously<sup>17</sup> allows evaluation of the time-dependent complex association/dissociation rates in monodisperse suspensions of soft colloidal ligand particles with arbitrary ratio between core radius and surface layer thickness. As such, the dynamic model covers the full spectrum of particle types, ranging from hard colloidal ligand particles to core/shell and polymeric (porous) particles with the limits of hard and porous particles as considered previously in refs 14 and 25, respectively.

Although theory in ref 17 highlights the basic aspects governing the kinetics of mixed chemical-diffusion controlled reaction between metal ions and soft colloidal ligand particles, it remains strictly applicable under the following conditions: (i) Ligands are homogeneously distributed within the colloidal shell; i.e., the soft interphase (Throughout the manuscript, the term “interphase” will be used rather than “interface” because the latter refers to an infinitely sharp plane separating soft colloidal shell and aqueous electrolyte. In practice, soft colloids, microorganisms in particular, are diffuse<sup>18,24</sup> with soft layer(s) characterized by a gradual transition of physical and chemical properties from bulk layer to electrolyte medium phase. To denote such a transition, the term “interphase” is more appropriate, and it further underpins the requirement for tackling the physical chemistry of soft particles on the basis of 3D phase properties whereas surface properties should be strictly invoked in the case of hard particles.) is represented according to a step-function-like profile. (ii) The impact of colloidal charge and resulting electric double layer (EDL) on the transport of free metal ions from bulk solution to the particle confined-ligands is neglected. Let us discuss how severe conditions i and ii are for aquatic colloidal systems.

Recent theoretical and experimental work on electrokinetics of environmental,<sup>18,21</sup> synthesized,<sup>19</sup> and biological soft colloidal particles<sup>22,23</sup> pointed out the necessity to picture the interphase between shell and aqueous medium as diffuse. Interphasial diffuseness basically means that the density of soft material constituting the shell is gradually distributed from the particle core to bulk electrolytic medium (see detailed discussions in refs 18 and 24). Such description of the soft interphase has been supported by experimental evidence<sup>26–32</sup> and is further fundamental for correctly addressing the response of the particle to changes in physicochemical conditions of the external medium (pH, ionic strength, temperature, solvent quality) or to external stimuli (electrical or mechanical constraints).<sup>26–35</sup> These factors possibly lead to anisotropic deformation of the shell in terms of particle swelling or shrinking.<sup>19,23,28,29,31–33,35</sup> The inhomogeneous distribution of soft polymeric material within the colloidal shell is inevitably accompanied by a diffuse repartition of the ligand sites it carries. These sites are often responsible for the overall (titrable) charge carried by the particle (e.g., carboxyl and phenolic groups for humic acids).<sup>19–21</sup> Because of the inherent dependence of the distribution of polymer chains on salt level and solvent quality (coil or collapsed colloidal state<sup>23,24,26–32</sup>), it is anticipated that ligand distribution within soft colloidal particles dispersed in river or seawater will be fundamentally different with consequences for the dynamics of metal speciation that have been so far completely unexplored. Also, it is mentioned that the very details of the spatial distribution for the soft material density are likely to be governed by the very binding of the metal ions to the reactive sites located in the shell, via, e.g., the formation of intramolecular bridges and resulting modifications of local chain conformation.<sup>36</sup> Finally, for some biological systems such as bacteria and viral particles, the complexity of the cell wall and/or internal

composition of the particle requires taking into account, besides the physical heterogeneity invoked above, a chemical heterogeneity associated to the spatial repartition of ligand sites of different natures throughout the particle reactive volume.<sup>22</sup>

Regarding the neglect made in refs 14 and 17 of the impact of colloidal charge on metal speciation dynamics, it is reasonable under conditions of sufficiently large salt level in aqueous medium, i.e., for significant screening of the colloidal charge by ions present in the electrolytic phase. Also it is acceptable when the charge carried by the particle is so low that interfacial electrostatic potentials remain well below  $k_B T/e$  with  $k_B$  the Boltzmann constant,  $T$  the temperature, and  $e$  the elementary charge. Natural organic matter and micro-organisms are generally negatively charged. The ionogenic sites responsible for this charge are not only likely to bind and affect the fate of charged metallic species but also to impact their spatial distribution around the particle via the action of the interphasial electric field that originates from electric double layer formation. Humic acids<sup>21</sup> may exhibit local inner electrostatic potentials in the range  $\sim -100$  to  $\sim -80$  mV for 10–100 mM solution ionic strength, with as a result a significant electrostatic partitioning of cations throughout the particle interphase. The extraordinary diversity in microbial life forms offers a wide spectrum of electrostatic characteristics defining these microorganisms, with, e.g., volume charge densities in the range  $-1$  to  $-100$  mM and above<sup>18,22–24</sup> (charge expressed in molar concentration of equivalent charges).

Given the above elements, the current study reports a theoretical formalism for metal speciation dynamics in suspensions of diffuse, charged soft colloidal ligand particles, thereby extending the approach detailed in ref 17 to situations of practical interest where EDL and heterogeneous ligand distributions within the colloidal shell are expected to impact on the overall metal flux to the reactive particle.

## 2. Theory

**2.1. Modeling the Soft Diffuse Interphase between Soft Colloidal Ligand Particle and Aqueous Electrolyte.** By adoption of the nomenclature introduced in ref 17, the soft colloidal particles consist of a rigid core of radius denoted as  $a$ , strictly impermeable to solvent molecules and ions, and a soft permeable colloidal shell of thickness  $d$ , as schemed in Figure 1. The particles are positioned according to a Kuwabara cell representation (Figure 1A) where each particle is surrounded by a virtual cell of radius  $a + r_c$  with  $r_c > d$ . The particle/solution volume ratio in a unit cell equals the particle volume fraction over the entire system so that the dimension  $r_c$  is given by

$$r_c = (a + d)\phi^{-1/3} - a \quad (1)$$

or, equivalently,

$$r_c = (4\pi c_p/3)^{-1/3} - a \quad (2)$$

with  $\phi$  the particle volume fraction (hard core and soft components included) and  $c_p$  the particle number concentration. Within the colloidal shell, the spatial distribution for the density  $n_s$  of constituting polymer segments is assumed to depend on the radial position  $r$  only (the origin is taken at the center of the particle core) according to the relationship

$$a \leq r \leq a + d: \quad n_s(r)/n_s^* = f(r) \quad (3)$$

where  $f$  is a radial function that satisfies the conditions  $f(r=a+d) = 0$  and  $df(r)/dr|_{r=a+d} = 0$ , which express the vanishing of the

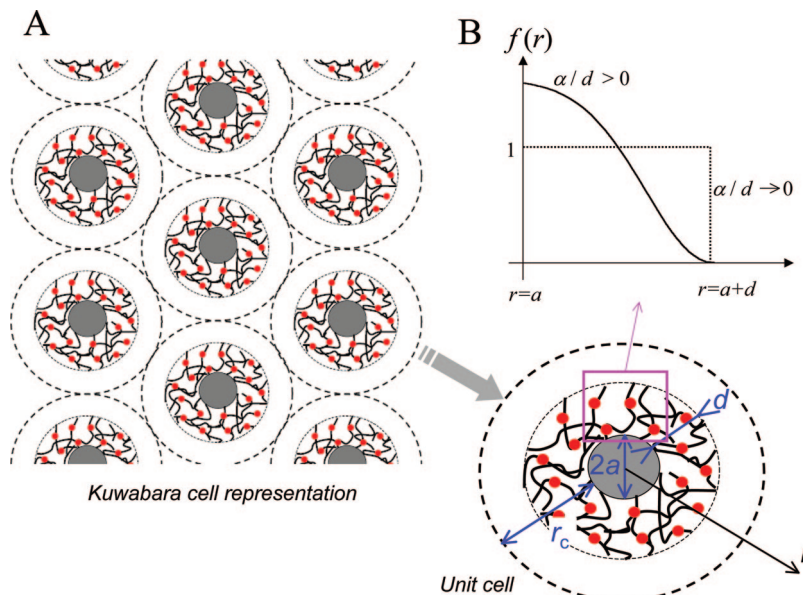


**Figure 1.** (A) Scheme (not to scale) of a dispersion of monodisperse soft colloidal ligand particles distributed according to a Kuwabara cell type representation. The unit cell of this representation is given with the indication of the nomenclature used for the coordinate system and for the geometrical parameters that define the particles. (B) Schematic representation of the radial ligand distribution profile within the soft surface layer for homogeneous ( $\alpha/d \rightarrow 0$ ) and diffuse ( $\alpha/d > 0$ ) ligand repartition.

polymeric shell at the very interface formed with the electrolytic medium.  $n_s^*$  is the nominal segment density,<sup>24</sup> i.e., for homogeneous distribution of soft material within the shell phase. As extensively discussed previously,<sup>18,24</sup> the determination of the function  $f$  requires knowing the types and magnitudes of the interactions existing in the system {charged polymer segments—solvent molecules—electrolyte ions}. Although such information is accessible for rather simple microgel particles or gel films using, e.g., light scattering measurements,<sup>26–31</sup> it is not easily at hand for complex biological systems<sup>23</sup> except perhaps for bacteriophages.<sup>22</sup> For this reason and for the sake of illustration, we shall adopt in the following a Gaussian-like distribution for the polymer segment density profile, i.e.

$$\begin{cases} a \leq r \leq a+d: & f(r) = \chi \left\{ 1 - \exp\left(-\left[\frac{r-(a+d)}{\alpha}\right]^2\right) \right\} \\ a+d \leq r \leq a+r_c: & f(r) = 0 \end{cases} \quad (4)$$

where  $\alpha$  corresponds to the typical length over which the radial segment density distribution decays. The magnitude of the ratio  $\alpha/d$  informs on the extent of diffuseness of the interphase. Although the situation of step-function profile is recovered for  $\alpha/d \rightarrow 0$  (which corresponds to  $n_s(r)/n_s^* \rightarrow 1$ ), increasing values of  $\alpha/d$  lead to a pronounced position dependence for  $f$  or, for that matter  $n_s$  (see Figure 1B). To achieve a correct understanding of the effect of segment density on speciation dynamics, the parameter  $\chi$  in eq 4 ensures the constancy of the total polymer segment concentration<sup>24</sup> or, equivalently, of the total concentration of ligand sites upon changing  $\alpha/d$  and/or  $d$ . It is therefore provided by

$$\chi = \frac{(a+d)^3 - a^3}{3 \int_a^{a+d} r^2 \left\{ 1 - \exp\left(-\left[\frac{r-(a+d)}{\alpha}\right]^2\right) \right\}} \quad (5)$$

It is stressed that the calculations below will be carried out using the radial density profile as defined by eqs 3–5. Such profiles have been measured by neutron reflectivity on weak ionic polymer brushes<sup>28,30,31</sup> and are theoretically predicted for poly-

electrolyte brushes in osmotic regime.<sup>30,31,37</sup> Without loss of generality, our formalism below is valid for any other profile  $f(r)$  whether empirical, analytical, or computational.<sup>24,38,39</sup> Note that the radial density distribution given in eq 4 is not that adopted in ref 24 within the framework of electrophoresis theory for infinitely dilute suspensions of diffuse soft colloids. We motivate this by arguing that the profile defined in eq 4 enables an unambiguous positioning of the edge of the shell (located at  $r = a + d$ ), whereas the tanh-like function introduced in ref 24 inevitably requires defining the limit of extension of the shell layer according to arbitrary prescribed quantitative criterion.<sup>40</sup>

For the sake of simplicity, it is assumed that the soft particles under consideration carry a single type of ligands L of charge  $z_L e$  with  $z_L$  the valency of L. By assumption that ligands L within the colloidal shell are uniformly distributed along the polymer chains, the local ligand concentration, denoted as  $c_L(r)$ , verifies

$$a \leq r \leq a+d: \quad c_L(r)/c_L^* = f(r) \quad (6)$$

where the nominal ligand concentration  $c_L^*$  is linearly related to  $n_s^*$  via  $c_L^* = n_s^* \Theta / N_A$ , where  $\Theta$  is the number of binding sites per polymer segment and  $N_A$  is the Avogadro number. Within the soft surface layer, the space charge density distribution  $\rho_L^{\text{el}}(r)$  stemming from the presence of charged sites L is simply given by

$$a \leq r \leq a+d: \quad \rho_L^{\text{el}}(r) = z_L F c_L^* f(r) \quad (7)$$

Equation 7 is valid under the condition that protolytic dissociation of the charged reactive sites L is complete. In reality, the degree of dissociation of these may depend on the concentration in solution of so-called charge-determining ions for the particle considered (e.g., protons/hydroxyls for L representing carboxylic or phenolic functional groups as in humic substances<sup>21</sup>). Also, the local electrostatic potential distribution  $\psi(r)$  within the shell is known to impact the dissociation of ionogenic sites and thereby the overall titrable charge carried by the particle.<sup>19</sup> In recognition of these elements, eq 7 should be then replaced by<sup>19,24</sup>



$$a \leq r \leq a + d: \quad \rho_L^{\text{el}}(r) = z_L F c_L^* f(r) g(\text{pH}, \psi(r)) \quad (8)$$

where  $g$  is an isotherm describing the protolytic properties of the polyelectrolyte layer where charged  $L$  are distributed. For the sake of simplicity and conciseness, eq 7 will be that used in the following developments. It is stressed that examination of cases where colloidal charge is mediated by bulk concentration of charge-determining ions and salt level in solution may be straightforwardly done adopting corrections of the type indicated in eq 8.

**2.2. Formulation of the Problem.** Consider a swarm of identically charged diffuse soft colloidal ligand particles described above and distributed in dispersion as shown in Figure 1. The aqueous medium contains a  $z:z$  symmetrical indifferent background electrolyte at concentration  $c^\infty$ . The indifferent nature of the electrolyte ensures the absence of any chemical reaction between ligands  $L$  and anions/cations present in solution. Once the electric double layer as originating from the charge carried by the particles is completely relaxed, i.e., anions/cations distributions within and outside the soft particle have reached thermodynamic equilibrium (this generally requires time delays of the order of the microseconds<sup>41</sup>), metal ions ( $M$ ) of valency  $z_M$  are introduced in the medium at initial bulk concentration denoted as  $c_M^*$ . This operation defines our reference state for the time scale, i.e.,  $t = 0$ . Metal ions ( $M$ ) are then supposed to interact with the particle-confined ligands according to the reaction



where  $k_a$  and  $k_d$  are the intrinsic  $ML$  complex association and dissociation rate constants, respectively. The intrinsic (chemical) stability constant  $K$  of the  $ML$  complex is provided by  $K = k_a/k_d$ . The magnitude of the rate constant  $k_a$  is generally in agreement with the Eigen mechanism<sup>42</sup> that comprises the formation of a precursor outer-sphere complex, with an electrostatically determined stability ( $K_{os}$ ), followed by removal of water from the inner coordination sphere ( $k_w$ ) as the usual rate-limiting step.<sup>43</sup> The association rate constant is then given by

$$k_a = K_{os} k_w \quad (10)$$

The stability constant  $K_{os}$  for the outer sphere is primarily dependent on the charges of the reacting species and on the ionic strength of the medium. A theoretical expression for  $K_{os}$  that includes both local electrostatic interactions between  $M$  and  $L$  and the effect of ionic strength on those interactions may be derived from statistical considerations.<sup>42</sup> The result reads as

$$K_{os} = \frac{4\pi}{3} N_a a_g^3 \exp\left(-\frac{z_M z_L e^2}{4\pi\epsilon_0 \epsilon_r T a_{cc}} \left[1 - \frac{\kappa a_{cc}}{1 + \kappa a_{cc}}\right]\right) \quad (11)$$

which is based on the combination of the Fuoss equation<sup>44</sup> with Debye–Hückel electrostatics for the point charge interaction with inclusion of screening by the surrounding electrolyte solution. In eq 11,  $\epsilon_0$  and  $\epsilon_r$  are the dielectric permittivity of vacuum and relative dielectric permittivity of the medium, respectively,  $a_g$  is the geometrical center-to-center distance between  $M$  and  $L$ ,  $a_{cc}$  is the charge center-to-center distance between  $M$  and  $L$ , and  $\kappa$  the reciprocal screening Debye layer thickness defined by

$$\kappa = \left(\frac{2z^2 F^2 c^\infty}{\epsilon_0 \epsilon_r RT}\right)^{1/2} \quad (12)$$

Equation 12 holds for aqueous solutions where the inequality  $c^\infty \gg c_M^*$  is satisfied; i.e., the indifferent background electrolyte is in

large excess over the target metal ions. For the sake of simplicity, we shall ignore the difference between the mass and the charge separations between metal ion and ligand. As correctly pointed out in ref 45, this approximation is expected to be crude when considering composite molecular ligand systems. It is specified here that van Leeuwen<sup>46</sup> recently derived a formalism showing that Eigen mechanism generally continues to apply for the situation of a 2D/3D surface/colloid-bound ligand sites, but it does so for a  $K_{os}$  value different from that relevant for freely dissolved ligands (eq 11). The discrepancy mainly originates from differences in complex geometry, but the conceptual electrostatic and screening corrections necessarily involved in the expression of  $K_{os}$  remain basically the same as those appearing in eq 11. In the current study, for the sake of generality and simplicity, we do not specify the nature of the ligand particle (that can be a microgel particle, a biocolloid, etc.) and the detailed geometry of the complex within the ligand particle, and thus we reason on the basis of eq 11. Depending on the type of complexing colloid considered, refinement of  $K_{os}$  is possible as detailed in ref 46, and subsequent implementation in our metal speciation dynamics formalism is straightforward. Also, for a certain metal complex of which the formation does not follow the conventional Eigen mechanism, eqs 10 and 11 have to be replaced by expressions in line with the so-called generalized Eigen mechanism.<sup>47</sup>

### 2.3. Key Transport Equations Governing the Local $M$ and $ML$ Concentration Profiles in Colloidal Ligand Suspensions.

**Validity Frame for the Dynamic Speciation Model.** Before writing explicitly the fundamental transport equations that govern the temporal and spatial dependencies of the local concentrations of  $M$  and  $ML$  within and outside the soft colloidal ligand particles, we find it of utmost importance to first consider explicitly the various assumptions that underly their validity. Some of these have already been thoroughly discussed,<sup>17</sup> and the reader is referred to ref 17 for further details.

Below, we shall consider that  $D_{\text{particle}} \ll D_M$  where  $D_{\text{particle}}$  and  $D_M$  stand for the diffusion coefficient of the particle and free metal ions, respectively. This imposes a lower particle size limit of the order 2–5 nm below which our developments cannot be applied. Besides, we neglect sedimentation rates, so that particles of upper size-limit 1–10  $\mu\text{m}$  will be considered.<sup>17</sup> Also, continuum (smeared out) electrostatic (mean field Poisson–Boltzmann formalism) and diffusion equations will be employed, thus examining situations where  $l \ll d$  and/or  $\kappa l \ll 1$ ,  $l$  being the typical separation distance between two adjacent reactive sites. As extensively discussed,<sup>17</sup> the motion of ligands  $L$  or for that matter  $ML$  complex within the shell layer is disregarded and the ligand distribution within the shell is considered frozen in time. Besides, within the scope of the current analysis, we shall tackle the situation of unstirred aqueous media (convection free) with a large excess of indifferent background electrolyte over  $M$  species, and a large excess of  $L$  sites over free  $M$  ions for every position  $r$  within the colloidal shell. This allows us (i) to maintain a prescribed constant value for the total ionic strength of the medium, (ii) to neglect the impact of  $M$  concentration (that varies in space and time) on the electric double layer (EDL) composition, the latter being primarily governed by the pre-equilibrated distributions ( $t < 0$ ) of indifferent electrolyte ions throughout the soft interphase, (iii) to disregard the change with time of the local ligand concentration due to reaction (9) and thereby that of the volume charge density of the particle (see eqs 6–8), and finally (iv) to identify the diffusion of the free metal species outside and within the electric field set up by the EDL as the predominant mode of transport with quickly achieved steady state for particles with

sizes ranging from 2–5 nm to 1–10  $\mu\text{m}$ .<sup>48–51</sup> Note that simplifications i–iv are generally in agreement with practical environmental situations of interest where metals are present at the state of traces<sup>1</sup> and are in interaction with highly charged colloidal matter. In situations where these requirements are not met, the current formalism should be amended for taking into account the coupled relaxation of the EDL (relaxation toward equilibrium) via the mixed transport-kinetic contributions that govern the local concentrations of indifferent ions and target metal across the interphase. In such situations, it may well be that complexation by shell ligands and associated re-equilibration of the EDL become competitive parallel processes. This situation of EDL relaxation mediated by intraparticle complexation reactions is currently under theoretical and experimental investigations.

In the following, we shall exclusively investigate cases where  $r_c \gg a + d$  and  $\kappa r_c \gg 1$ . The latter condition warrants the absence of EDL overlap between neighboring particles. The former ensures that the concentration profiles in the nonequilibrium chemical regime are at steady state, while the bulk metal concentration is being possibly depleted (for discussion on this issue, see ref 9 and Supporting Information therein). We stress, however, that the model and numerical analysis reported here are sufficiently complete to cover practical situations where the conditions  $r_c \gg a + d$  and  $\kappa r_c \gg 1$  are not necessarily satisfied. It is underlined that the extent of validity of the condition  $c_L(r) \gg c_M^*$  ( $\forall r \in [a, a + d]$ ) depends on the position where radial density distribution is diffuse ( $\alpha/d > 0$ ). In particular, in the vicinity of  $r = a + d$ , this condition is necessarily violated because, in essence,  $c_L(r=a+d) = 0$ . This difficulty, also met within the classical homogeneous representation of ligand sites within the shell,<sup>14,17,25</sup> is here circumvented by ignoring the very time variation of L concentration in particular at  $r \approx a + d$ .<sup>17</sup> This is legitimate as long as the condition  $c_L(r) \gg c_M^*$  applies for  $r = (a + d)^-$ , which is rendered possible by the choice of the profile  $f(r)$ . Also, the interfacial distance over which  $c_L(r)$  increases from 0 to values larger than  $c_M^*$  is of the order  $l$ , and hence this issue is one of the details in the transient regime.

**Local Transport Equations for M and ML Species.** Under the conditions given above, M species diffusion within/outside the particle shell and M species conduction under the action of the EDL interphasial field are the metal transport modes to be considered. The conservation equations for M and ML within a unit cell are then given by

$$a \leq r < a + d:$$

$$\begin{cases} \frac{\partial c_{ML}(r,t)}{\partial t} = -\{k_d c_{ML}(r,t) - k_a c_M(r,t) c_L^* f(r)\} \\ \frac{\partial c_M(r,t)}{\partial t} = D_M \nabla_r^2 c_M(r,t) + \{k_d c_{ML}(r,t) - k_a c_M(r,t) c_L^* f(r)\} \\ \quad + \frac{z_M D_M}{z} \left\{ \frac{\partial c_M(r,t)}{\partial r} \frac{\partial y(r)}{\partial r} + c_M(r,t) \nabla_r^2 y(r) \right\} \end{cases} \quad (13,14)$$

$$a + d \leq r \leq a + r_c:$$

$$\begin{aligned} \frac{\partial c_M(r,t)}{\partial t} &= D_M \nabla_r^2 c_M(r,t) + \\ &\frac{z_M D_M}{z} \left\{ \frac{\partial c_M(r,t)}{\partial r} \frac{\partial y(r)}{\partial r} + \tilde{c}_M(r,t) \nabla_r^2 y(r) \right\} \end{aligned} \quad (15)$$

where  $c_{i=M,ML}(r,t)$  is the local concentration of species  $i$  at a given time  $t$  and radial position  $r$  and  $\nabla^2 \equiv \partial^2/\partial r^2 + (2/r)\partial/\partial r$

is the Laplacian operator in spherical geometry. The diffusion coefficient of free metal species,  $D_M$ , is taken identical within and outside the particle shell under conditions set forth previously.<sup>17</sup> The quantity  $y(r)$  is the dimensionless local EDL potential defined by  $y(r) = zF\psi(r)/RT$  with  $F$  the Faraday number and  $R$  the gas constant.

The capture of the physical meaning of eqs 13–15 deserves some additional comments in conjunction with the conditions discussed above which warrant the validity of the proposed dynamic speciation model. In eq 13, the term related to ML diffusion is ignored in line with  $D_{\text{particle}} \ll D_M$  and the neglect of the motion of L/ML groups within the particle, as previously discussed. Doing so, the remaining term is the chemical source term due to complex association and dissociation that govern the variations in time and space of  $c_{ML}(r,t)$  within the particle shell. Equation 14 is the time-dependent Nernst–Planck equation where diffusion, chemical source term, and conduction components are included. Because we are examining practical situations where  $c^\infty \gg c_M^*$  and  $c_L(a \leq r < a + d) \gg c_M^*$ , the electric double layer maintains its equilibrium state (achieved at  $t < 0$ ) during the speciation experiment. As such, EDL composition and electric potential  $y$  both remain independent of the space and time concentration variations of M and ML within and/or outside the colloidal shell. Because of the absence of ligand sites outside the shell, the chemical source term is not present in eq 15. Finally, the excess of ligands over free metal ions allows us to disregard the time variation of local ligand concentration  $c_L(r) (=c_L^* f(r))$  in eqs 13 and 14.

**Boundary Conditions for Free and Bound Metal Concentrations.** At  $t = 0$ , the soft particles with ligands L and equilibrated EDL get into contact with aqueous solution that contains free metal species M at initial bulk concentration  $c_M^*$ . The initial free and bound metal concentrations within the particle shell are set to zero, which gives

$$c_{ML}(a \leq r \leq a + d, t=0) = 0 \quad (16)$$

$$c_M(a \leq r \leq a + d, t=0) = 0 \quad (17)$$

whereas outside the shell where there is necessarily no complex ML, we write

$$c_M(a + d \leq r \leq a + r_c, t=0) = c_M^* \quad (18)$$

The author verified that the nature of the initial eqs 16–18 do not impact the M and ML concentration profiles once they have reached the quasi-steady-state regime, i.e., the regime where the diffusive flux of free M outside the shell layer maintains its steady-state nature. It is in this regime that the dependence of the effective colloidal complex association–dissociation rates and of the colloid complex stability constant will be analyzed as a function of electric double layer field. In particular, substituting the right-hand sides of eqs 16–18 by the appropriate thermodynamic expressions for the local M and ML concentrations, as required within the context of dielectric relaxation analysis, leaves unchanged the speciation dynamic parameters of interest in the quasi-steady-state regime. In other words, the nature of eqs 16–18 falls in the details of the transient regime.

The required four spatial boundary conditions related to eqs 14 and 15 and pertaining to M concentration within and outside the soft surface layer, are given by

$$\partial c_M(r,t)/\partial r|_{r=a,t} = 0 \quad (19)$$

$$\partial c_M(r,t)/\partial r|_{r=a+r_c,t} = 0 \quad (20)$$

$$\mu_M(r=a+d^-,t) = \mu_M(r=a+d^+,t) \quad (21)$$

$$\left\{ \partial c_M(r,t) / \partial r + \frac{z_M}{z} c_M(r,t) \frac{\partial y(r)}{\partial r} \right\}_{r=a+d-,t} = \left\{ \partial c_M(r,t) / \partial r + \frac{z_M}{z} c_M(r,t) \frac{\partial y(r)}{\partial r} \right\}_{r=a+d+,t} \quad (22)$$

Equation 19 reflects the impermeable character of the core particle surface for free metal species, and eq 20 stems from symmetry consideration for the M concentration profile at the position that corresponds to half the separation distance between centers of two adjacent particles. Equations 21 and 22 are the required continuity equations for the electrochemical potential of M and for the overall flux of M (diffusion and migration components included) at the edge of the shell layer, respectively. Note that combining eqs 21 and 22 with the necessarily verified continuity equations for the EDL field and electrostatic potential at  $r = a + d$  (see following alinea) leads to the continuity of the M concentration profile and its derivative at  $r = a + d$ . The requirements imposed on the polymer segment density profile at  $r = a + d$  ( $f(r=a+d) = 0$  and  $df(r)/dr|_{r=a+d} = 0$ ) allows a formulation of the problem in a single continuous domain  $r \geq a$ , as extensively discussed in the Supporting Information.

**Determination of the EDL Field.** Within the common assumptions that solvent-mediated forces may be neglected and that the different ionic species are pointlike, the distribution of the (indifferent) electrolyte ions at equilibrium obeys Boltzmann statistics and the equilibrium potential  $\psi$  the nonlinear Poisson–Boltzmann equation, both being function of the radial position only. Thus it comes for a  $z:z$  symmetrical electrolyte

$$\nabla^2 y(r) = -\frac{zF}{RT\epsilon_0\epsilon_r} \{ \rho_{\text{ions}}^{\text{el}}(r) + \rho_L^{\text{el}}(r) \} \quad (23)$$

with

$$\rho_{\text{ions}}^{\text{el}}(r) = -2zFc^\infty \sinh(y(r)) \quad (24)$$

$\rho_{\text{ions}}^{\text{el}}(r)$  pertains to the local space charge density associated with mobile indifferent ions distributed throughout the core–shell/aqueous medium interphase, and  $\rho_L^{\text{el}}(r)$  is that originating from fixed charged ligand sites distributed according to the radial density profile given by eq 4.

The continuous formulation of the function  $f(r)$  for radial positions ranging from  $r = a$  to  $r = a + r_c$  (in particular at  $r = a + d$ , see eq 4) avoids the necessity for introducing other boundaries than those pertaining to the core–shell interphase ( $r = a$ ) and the far-field domain ( $r = a + r_c$ ).<sup>24</sup> The former reflects the electrosurface properties of the particle core and may be written in terms of the particle core surface potential, core surface charge or regulation mechanism,<sup>24</sup> depending on the chemical nature of the particle core considered. For simplicity, we shall here exclusively examine situations where the particle core surface is uncharged, so that

$$\left. \frac{\partial y(r)}{\partial r} \right|_{r=a} = 0 \quad (25)$$

Straightforward modifications of eq 25 may be done, e.g., when examining particles of which the core surface charge is pH-dependent or the core surface potential is Nernst-like (see refs 19 and 24 for further details). The boundary for cell–cell contact is given by

$$\left. \frac{\partial y(r)}{\partial r} \right|_{r=a+r_c} = 0 \quad (26)$$

and originates from symmetry of the electrostatic potential at half the center-to-center separation distance between adjacent

particles. In the absence of EDL overlap, that is, for  $\kappa r_c \gg 1$  (case considered in this study), eq 26 is equivalent to setting  $y(r \rightarrow \infty) = 0$ , which basically translates bulk electroneutrality condition.

**2.4. Derivation of the Effective Kinetic Rate Constants  $k_a^*$  and  $k_d^*$ .** The quantitative derivation of the effective complex association and dissociation rate constants (denoted as  $k_a^*$  and  $k_d^*$ , respectively), which are relevant at the scale of the ligand particle or for that matter of the unit cell where it is enclosed, necessarily requires correcting the local kinetic rate constant  $k_a$  and  $k_d$  by the appropriate transport contributions underlying the interaction of M with the colloidal ligand particle. The rate constants  $k_a^*$  and  $k_d^*$  should verify the conservation equations that are now written for a colloidal particle within a unit cell<sup>17</sup>

$$\frac{\partial \rho_{i=M,ML}^V(t)}{\partial t} = \pm \{ k_d^* \rho_{ML}^V(t) - k_a^* \rho_M^V(t) \rho_L^V \} \quad (27)$$

The + sign at the right-hand side of eq 27 holds for  $i = M$  and the – sign for  $i = ML$ . The M, ML, and L concentrations  $\rho_{i=M,ML}^V(t)$  and  $\rho_L^V$  over the whole cell volume are defined by

$$i = M, ML: \quad \rho_i^V(t) = \frac{4\pi}{V_c} \int_a^{a+r_c} r^2 c_i(r,t) dr \quad (28)$$

and

$$\rho_L^V = \frac{4\pi}{V_c} \int_a^{a+r_c} r^2 c_L(r) dr = \frac{4\pi c_L^*}{V_c} \int_a^{a+d} r^2 f(r) dr \quad (29)$$

with  $V_c = 4\pi(a + r_c)^3/3 = c_p^{-1}$  the volume of a unit cell and  $c_p$  the particle number concentration introduced before (eq 2). Following the strategy previously adopted,<sup>17</sup> it may be shown that the searched  $k_a^*$  is depending on the time  $t$  and local rate constant  $k_a$  according to (see detailed derivation steps in the Supporting Information)

$$\frac{k_a^*(t)}{k_a} = \frac{\rho_M^s(t) \rho_L^V - \rho_{ML}^V(t) K^{-1}}{\rho_M^V(t) \rho_L^V - \rho_{ML}^V(t) K^{*-1}} \quad (30)$$

where the volume concentration of free metal within the shell layer at time  $t$ , denoted as  $\rho_M^s(t)$ , is defined according to

$$\rho_M^s(t) = \frac{4\pi}{V_s} \int_a^{a+d} r^2 c_M(r,t) f(r) dr \quad (31)$$

with  $V_s = 4\pi\{(a + d)^3 - a^3\}/3$  the volume over which the reactive binding sites L are distributed.

The colloid complex stability constant  $K^*$  involved in eq 30 is defined by  $K^* = k_a^*/k_d^*$  and is further provided by the explicit expression (see the Supporting Information for demonstration)

$$\frac{K^*}{K} = \frac{V_c}{V_s} \frac{\int_a^{a+d} r^2 f(r) \exp(-z_M y(r)/z) dr}{\int_a^{a+r_c} r^2 \exp(-z_M y(r)/z) dr} \quad (32)$$

Equation 32 corrects the intrinsic (chemical) ML complex stability constant  $K$  for the electrostatic contribution arising from the EDL field and for the heterogeneous ligand distribution within the colloidal shell. Note that the EDL field and potential both intrinsically depend on the charged ligands distribution within the shell, as underlined by eqs 23 and 24 and eq 7. In the case where screening of colloidal charge by ions from background electrolyte is complete (as met for sufficiently large electrolyte concentrations), we have  $y(r) \rightarrow 0$ . By combination of eq 32 and eqs 4 and 5 for such cases, we get



$$K^* \rightarrow K \quad (33)$$

Equation 33 corresponds to the limiting situation analyzed previously,<sup>17</sup> where EDL electrostatics was not taken into account within metal speciation dynamics formalism.

**2.5. Computation Procedure and Analyses of Practical Limiting Situations. Numerical Scheme.** The set of eqs 13–26 rigorously defines the spatial profiles for the M and ML concentrations within (for ML and M) and outside (for M) the particle colloidal shell where ligands L are distributed. The details of the numerical procedure employed for solving eqs 13–26 and deriving the corresponding searched ratio  $k_a^*(t)/k_a$  (eq 30) are indicated in the Supporting Information. Following this procedure, the dependence of  $k_a^*(t)/k_a$  on the particle geometry (parameters  $a$  and  $d$ ), the background electrolyte concentration  $c^\infty$ , the nominal ligand concentration ( $c_L^*$ ), or the degree of interphasial diffuseness ( $\alpha/d$ ) may be obtained.

**Cases Where Analytical Expressions for  $K^*$  Are Available.** In view of the general expression that defines  $K^*$  (eq 32), the cases where explicit expressions for  $K^*$  are available are basically those where analytical derivation of the electrostatic potential distribution is possible. In the Debye–Hückel limit  $|y(r)| \ll 1$  under the condition  $\kappa r_c \gg 1$  (absence of EDL overlap), the Poisson–Boltzmann equations (eqs 23 and 24) may be linearized and solved analytically under the boundaries given by eqs 25 and 26. The electrostatic potential then reads as

$$y(x) = -\frac{1}{2(x + \kappa a)} \left\{ \int_0^{\kappa d} (x + \kappa a) \exp(-x) F(x) dx \right\} \times \\ \left\{ \exp(x) + \frac{\kappa a - 1}{\kappa a + 1} \exp(-x) \right\} + \\ \frac{\exp(x)}{2(x + \kappa a)} \int_0^x (x + \kappa a) \exp(-x) F(x) dx - \\ \frac{\exp(-x)}{2(x + \kappa a)} \int_0^x (x + \kappa a) \exp(x) F(x) dx \quad (34)$$

with  $x = \kappa(r - a)$  and  $F(x) = -(z_L c_L^*)/(2z c^\infty) k^2 f(x)$ . The combination of eq 32 with eq 34 defines the stability constant  $K^*$  of colloidal metal complexes for which  $|y(r)| \ll 1$ . The latter condition, which defines the degree of validity of eq 34, may be replaced by the more restrictive inequality  $|y(r=a)| \ll 1$  because the monotonous decrease of  $|y(r)|$  across the soft interphase basically imposes  $|y(r=a)| \geq |y(r)|$ .

**Cases Where Analytical Expressions for  $k_a^*$  Are Available.** We previously showed<sup>17</sup> that, in the nonequilibrium chemical regime, the complex association rate constant  $k_a^*$  may be satisfactorily approximated by

$$k_a^*/k_a \approx \left( 1 + \frac{k_a \rho_L^V}{4\pi(a+d)D_M c_p} \right)^{-1} \quad (35)$$

which holds for dilute suspensions of homogeneous soft particles ( $\alpha/d \rightarrow 0$ ) of which the size is significantly lower than the surrounding metal diffusion layer thickness (condition satisfied as long as  $r_c \gg a + d^{17}$ ). The approximations leading to eq 35 are essentially the neglect of M and ML concentration polarizations within the shell layer and the neglect of the interphasial electric field across the soft interphase. The correctness of the former simplification was largely discussed in ref 17 upon comparison with rigorous numerical evaluation of  $k_a^*$  for  $y(r) \rightarrow 0$ . Following the basic steps which lead to eq 35 and which are detailed in ref 17 (see Appendix 5 therein), it is possible to easily modify eq 35 by including the enhancement of the free metal concentration within the shell layer as a result of the presence of a potential within the particle. After replacing the quantity  $c_M(r=a+d, t)$  in ref 17 by  $c^*(t) \exp(-z_M y(r=a+d)/z)$ ,

with  $c^*(t)$  the free metal concentration at time  $t$  just outside the electric double layer (where the potential is zero), we obtain

$$k_a^*/k_a \approx \exp(-z_M y(r=a+d)/z) \left( 1 + \frac{k_a \exp(-z_M y(r=a+d)/z) \rho_L^V}{4\pi(a+d)D_M c_p} \right)^{-1} \quad (36)$$

A similar expression was given in the conclusion of the work by Pinheiro et al.<sup>14</sup> who examined the case of hard ligand particles. Equation 36 is autoconsistent *only* in the limiting situations where a constant potential within the shell layer is physically realistic, that is, (i) for soft particles satisfying  $\kappa_m d \gg 1$  (thin EDL limit) and (ii) for soft particles satisfying  $\kappa d \ll 1$  (thick EDL limit); i.e., the soft layer recedes significantly within the EDL so that, from an electrostatic point of view, the particle may be viewed as a hard colloid. In case i,  $y(r=a+d)$  basically identifies to the Donnan potential  $y^D$ , and the quantity  $\kappa_m = \kappa \cosh(y^D)^{1/2}$  is the reciprocal Debye layer thickness within the shell layer corrected for electrostatics.<sup>52</sup> The Donnan potential  $y^D$  is simply evaluated from electroneutrality condition within the surface layer, thus yielding

$$y^D = \sinh^{-1} \left( \frac{z_L c_L^*}{2z c^\infty} \right) \quad (37)$$

In case ii,  $y(r=a+d)$  may be assimilated to the surface potential  $y(r=a)$ , for which Ohshima recently gave an implicit analytical formulation based on the resolution of transcendental integral equations.<sup>53</sup> It is stressed that eq 36 makes sense under the strict condition that the thickness of the EDL within and outside the particle is immaterial when compared to the thickness of the diffusion layer. Given this, we may state that the analogue in electrochemistry of eq 36 is the Frumkin formulation of electron transfer rates corrected for electric double layer effect.<sup>51</sup> Also, eq 36 basically relies on the simplistic electrostatic partitioning model of M species where the potential  $y$  is constant not only within the shell ( $y(r=a+d) = y^D$  for  $\kappa_m d \gg 1$  and  $y(r=a+d) \sim y(r=a)$  for  $\kappa d \ll 1$ ) but also just beyond the soft surface layer ( $y(r>a+d) = 0$ ). This comes to state that eq 36 essentially disregards the impact of the EDL field that develops within and beyond the shell. Appropriate account of the EDL field within the shell formalism for metal speciation dynamics in soft ligands suspensions necessarily requires inclusion of the nonlinear electrostatic terms (where the quantities  $\partial y(r)/\partial r$  and  $\nabla_r^2 y(r)$  are involved) in the fundamental M/ML transport equations (eqs 14 and 15).

### 3. Results and Discussion

**3.1. Impact of the EDL Interphasial Field on the M/ML Concentration Profiles and on the Time Dependence of  $k_a^*/k_a$ .** As a starting point, we first examine the basic features of metal speciation dynamics in dilute suspensions of soft colloidal particles with homogeneous distribution of ligands within the shell ( $\alpha/d \rightarrow 0$ , Figure 1B) as a function of the background electrolyte concentration  $c^\infty$ . The charge density carried out by the soft surface layer (eq 7) is set to  $\rho_L^V/F = -10$  mM ( $z_L = -1$ ), a value in agreement with that typically determined by electrokinetics for some polysaccharide microgel particles<sup>19</sup> or bioparticles.<sup>23</sup> Besides, the magnitude of this charge is sufficiently large to examine the contribution of EDL electrostatics on metal speciation dynamics for  $c^\infty$  values of practical interest, typically in the range 0.1–100 mM. For the sake of comparison, the M/ML concentration profiles and the time dependence of



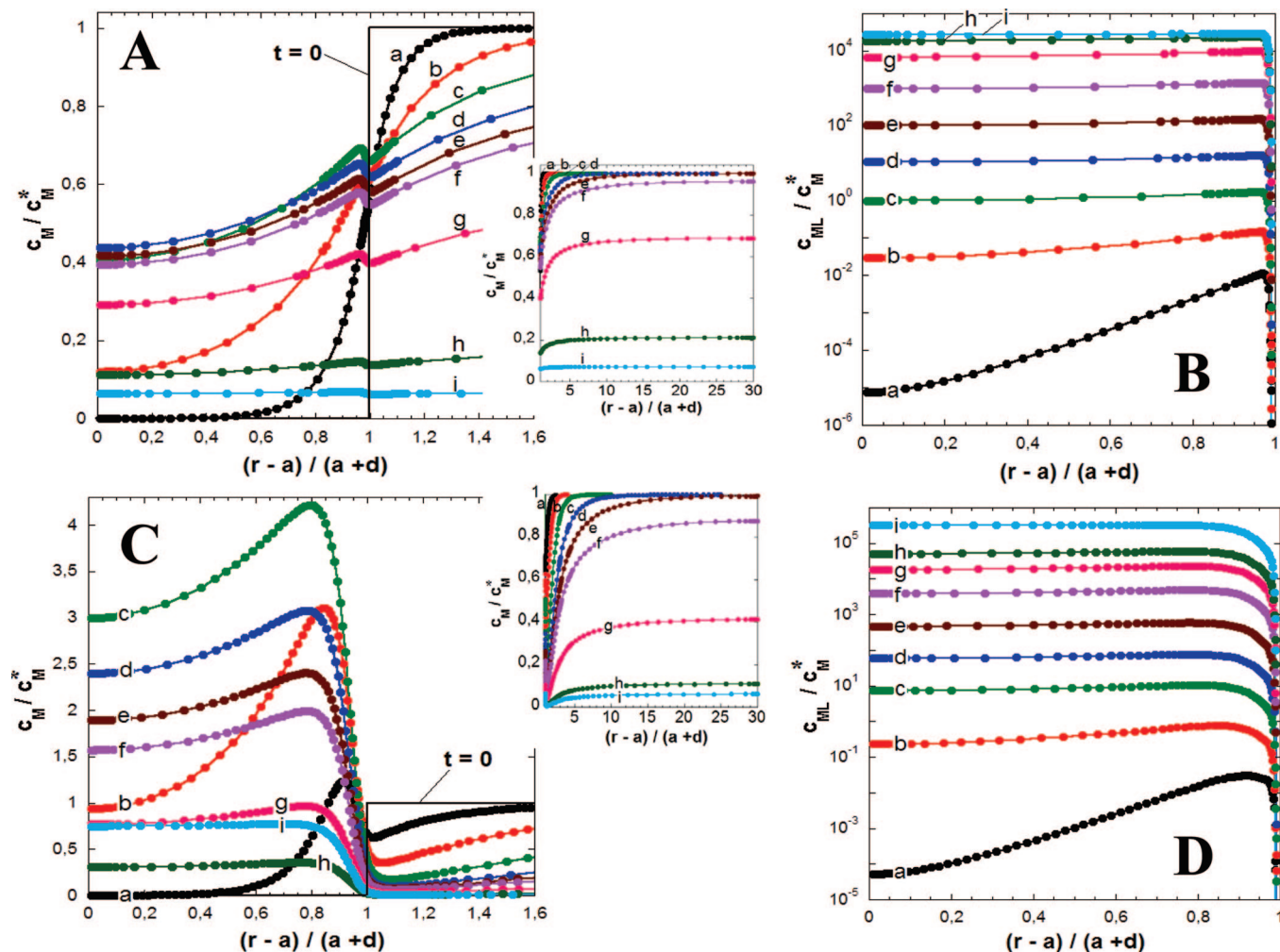


**Figure 2.** Typical concentration profiles for free metal M (panels A and C) and complex ML (panels B and D) species within and without the shell layer where ligands are located, at two electrolyte concentrations  $c^\infty = 100$  mM (panels A and B) and  $c^\infty = 0.1$  mM (panels C and D). In the insets of panels A and C, the M concentration profiles are depicted over the whole range of radial positions within the unit cell. Meaning of the symbols:  $t = 93$  ns (a), 0.93  $\mu$ s (b), 9.3  $\mu$ s (c), 93  $\mu$ s (d), 0.93 ms (e), 9.3 ms (f), 93 ms (g), 0.93 s (h), 9.3 s (i). The boundary between the soft shell layer and outer electrolytic medium is located at  $(r - a)/(a + d) \approx 1$ . Model parameters:  $d = 100$  nm,  $ad = 10^{-2}$ ,  $\alpha d = 10^{-2}$ ,  $D_M = 10^{-9}$  m<sup>2</sup> s<sup>-1</sup>,  $c_L^* = 10$  mol m<sup>-3</sup>,  $\rho_L^V = 3.7 \times 10^{-4}$  mol m<sup>-3</sup>,  $T = 298$  K,  $K = 5 \times 10^4$  mol<sup>-1</sup> m<sup>3</sup>,  $k_w = 7 \times 10^6$  s<sup>-1</sup>,  $K_{os} = 3.7 \times 10^{-3}$  mol<sup>-1</sup> m<sup>3</sup> =  $K_{os}(c^\infty = 10$  mM) (see related discussion in the main text),  $r_s/(a + d) = 30$ ,  $z = 1$ ,  $z_M = 2$ , and  $z_L = -1$ . The values of  $D_M$  and  $k_w$  are typical of those for Mn(II) metal ion,<sup>42</sup> and the value of  $K$  is typical of metal complexation by carboxylate groups distributed at the surface of latex particles.<sup>14</sup>

$k_a^*$  (Figures 2–4) at various  $c^\infty$  will be presented, in a first stage, for  $K_{os} = 3.7 \times 10^{-3}$  mol<sup>-1</sup> m<sup>3</sup> ( $z_L = -1$ ,  $z_M = +2$ ), thus ignoring the ionic strength dependence of  $K_{os}$  as expressed by eq 11. The adopted value for  $K_{os}$  corresponds to that for  $c^\infty = 10$  mM. In a second stage, the dependence of  $K_{os}$  with  $c^\infty$  will be explicitly taken into account, especially for analyzing the variation of  $k_a^*$  with  $c^\infty$  in the quasi-steady-state regime. This methodology allows unraveling the concomitant effects of the EDL interphasial field (relevant at the colloidal scale) and local inner electrostatic field (eq 11 relevant at the molecular scale or, for that matter, at the scale of the local ML complex) on the dynamic features of metal speciation in soft colloidal ligand suspensions.

In Figure 2, typical M and ML concentration profiles are depicted as a function of time for  $c^\infty = 100$  mM (parts A and B of Figure 2) and  $c^\infty = 0.1$  mM (parts C and D of Figure 2). At  $c^\infty = 100$  mM, departing from the situation at  $t = 0$  where M and ML species are absent from the particle shell (eqs 16 and 17), the ML concentration at a given position within the shell continuously increases with time as a result of gradual diffusion of free M from the solution (outside the particle) to the reactive shell layer and subsequent complexation (eq 9).

Doing so, the ML concentration at fixed time basically increases from  $r = (a + d)^+$  to  $r = (a + d)^-$ , thus following in this spatial region the profile dictated by the ligand distribution (Figure 1B). The concentration of ML complex then decreases from the inner edge of the soft surface layer ( $r = (a + d)^-$ ) to the interface core/shell ( $r = a$ ). This decrease is related to the corresponding decrease in free metal concentration as governed by diffusive transport of free M species outside and within the shell. The transitory development of the diffusion layer for the free M concentration at both sides of the very interface between the shell and the electrolyte solution (position  $r = a + d$ ) is reflected in the characteristic time evolution of the concentration profiles a–c in Figure 2A ( $0 < t < 10$   $\mu$ s). After some time delay ( $t > 5$  ms in the example commented here), bulk metal concentration significantly decreases with time as a result of metal depletion within the finite volume  $V_c$  (inset Figure 2A) where the soft colloidal ligand is located. This depletion is accompanied by a decrease with time of the local M concentration within the shell. It is thereby recalled that the difference between the rigorous no-flux condition as adopted in eq 20 and the approximate semi-infinite diffusion description remains insignificant as long as the typical depletion time scale is much larger than that for the

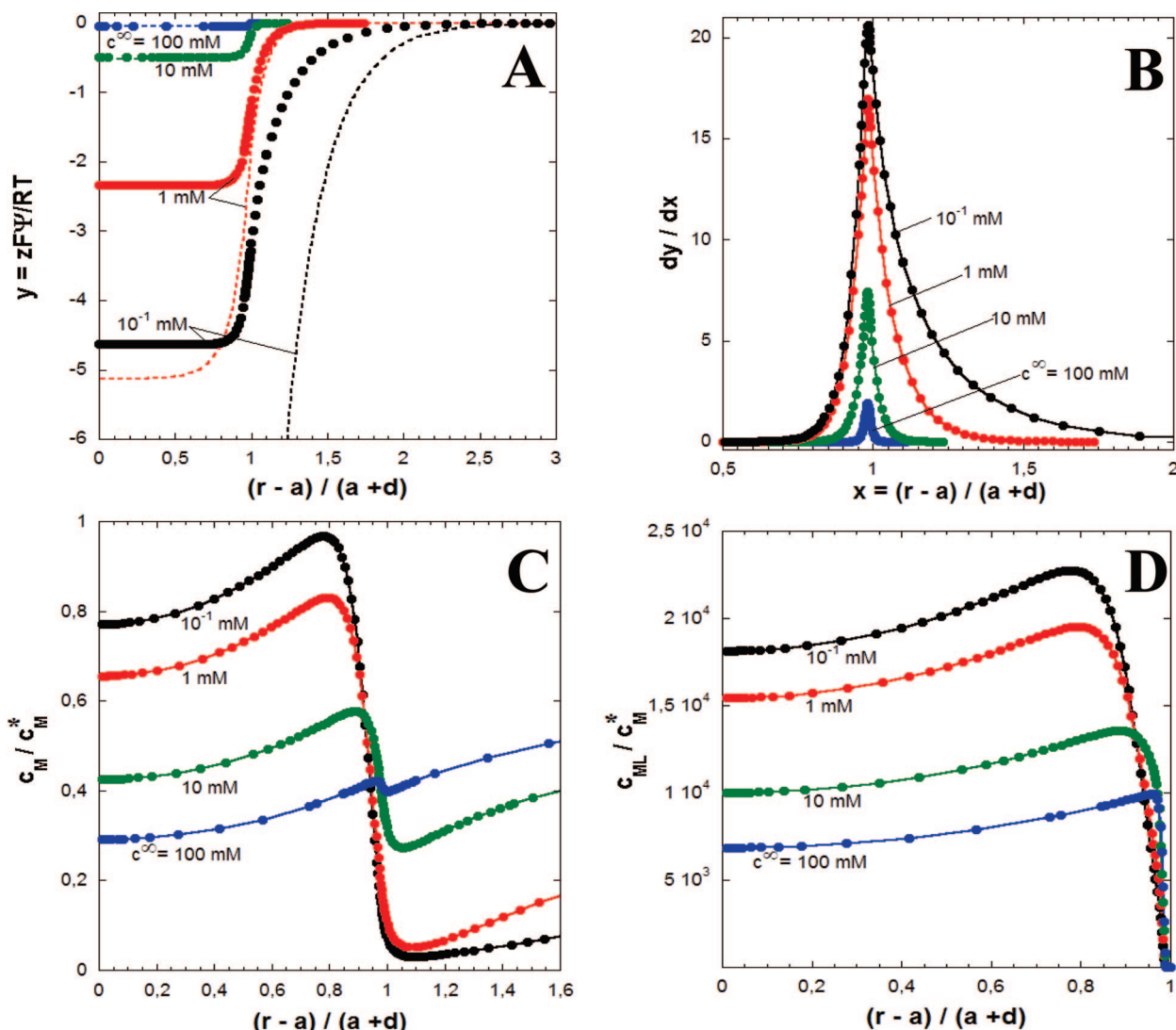


**Figure 3.** Distribution profiles for the dimensionless EDL electrostatic potential (panel A) and EDL field (panel B) at various electrolyte concentrations (indicated) under the conditions of Figure 2. Symbols refer to the exact solutions of the nonlinear Poisson–Boltzmann equation, and dotted lines in panel A are predictions based on the Debye–Hückel approximation (eq 34). Plain lines in panel B are only guides to the eye. Concentration profiles of free metal M (panel C) and complex ML (panel D) in the quasi-steady-state regime ( $t = 93$  ms) at various  $c^\infty$  (indicated) (same model parameters as in Figure 2).

establishment of the quasi-steady-state regime (or nonequilibrium chemical regime).<sup>9</sup> During the course of depletion, the M concentration gradient across the shell layer gradually vanishes and becomes nearly zero for sufficiently long time. Local chemical equilibrium within the soft particle surface layer is then reached,<sup>17</sup> and the M and ML local concentrations within the shell verify the thermodynamic equation

$$\frac{c_{ML}(r,t)}{c_M^*(r,t)} \rightarrow K \quad (38)$$

For  $c^\infty = 100$  mM, the fixed charges carried by the polymer chains in the shell are efficiently screened by the ions present in the indifferent electrolyte medium. As a result, the local equilibrium EDL potential and field strength are weak (parts A and B of Figure 3) with an electrostatic partitioning of the M species in the interphasial region core–shell/electrolyte that remains insignificant. This explains why at equilibrium (curve i in Figure 2A) the M concentration in the shell is essentially identical to that outside the soft particle. In parallel, the ML concentration distribution becomes flat, in line with eq 38. Along

with this, the stability constant  $K^*$  for the colloidal ML complex basically reduces to its intrinsic chemical component  $K$ . A closer inspection of the M concentration profiles in the time range that precedes the establishment of chemical equilibrium reveals that  $c_M$  slightly increases when passing from the position  $r = (a+d)^+$  to  $r = (a+d)^-$  before decreasing further inside the shell as commented above. This slight increase is due to the diffusion of M in the EDL region where the field, even weak, counteracts noticeably the diffusion process and the associated building up of interphasial M concentration gradient.

The latter features are magnified when examining the M/ML concentration profiles at  $c^\infty = 0.1$  mM (parts C and D of Figure 2). Here, for a given time  $t$ , the significant enhancement of the local M concentration from  $r = (a+d)^+$  (just outside the shell) to  $r = (a+d)^-$  is related to the strong magnitude of the potential within the soft surface layer (Figure 3A). This potential identifies to the Donnan potential because the thickness of the soft component of the particle considered in Figure 2 complies at  $c^\infty = 0.1$  mM with the condition of a thin EDL. The coupling between the free metal diffusion process and the migration of

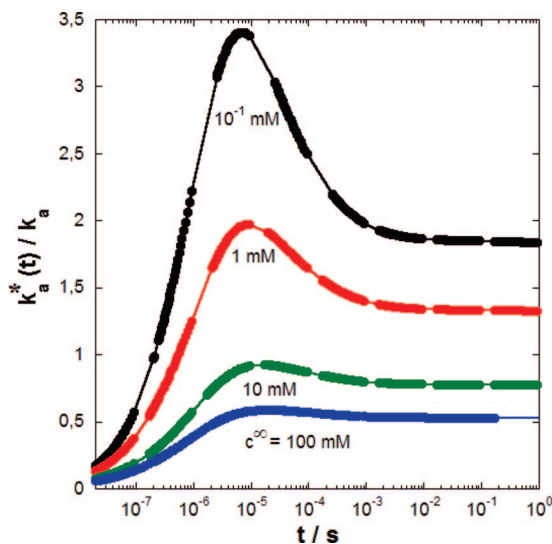


**Figure 4.** Time dependence of the ratio  $k_a^*(t)/k_a$  in the transient and quasi-steady-state regimes under the conditions of Figure 2, at various  $c^\infty$  (indicated). Plain lines are only guides to the eye.

M in the EDL region results in peculiar concentration profiles marked by a maximum that grows in the transient regime (curves a–c) during the formation of the M diffusion layer and further diminishes in magnitude when bulk metal depletion starts to significantly set in (curves d–h in the inset of Figure 2C). For a sufficiently long time, i.e., upon approach of chemical equilibrium (eq 38), this maximum basically disappears (see curves f–i) as a result of the nearly completed balance between diffusion and migration transport of M within the shell layer. It is then observed that the interphasial Donnan partitioning for M is so strong that it leads to an increase of the local M concentration inside the shell till Boltzmann equilibrium profile is reached (curves h and i in Figure 2C). This latter increase in local M concentration, purely electrostatic in nature, opposes to the decrease of  $c_M$  in the depletion regime (governed by diffusion and migration transports), which precedes the setting of local chemical equilibrium. Overall, the strong EDL potential and field strength at the colloidal ligand interphase lead to an efficient pumping of free metal ions into the shell. For decreasing  $c^\infty$ , this results, at a given  $t$ , in larger local ML concentration within the shell, as inferred from comparison of local ML distribution profiles obtained at 0.1 mM (Figure 2D) and 100 mM (Figure 2B). Also, related to this, it is noteworthy that depletion of M within the unit cell is accelerated by the presence of the EDL field (insets of parts A and C of Figure 2) and that the larger the electrolyte concentration, the faster chemical equilibrium is established (see discrepancies between curves h and i in parts B and D of Figure 2). In agreement with the strong EDL potential (in absolute value) at  $c^\infty = 0.1$  mM, the magnitude of the electrostatic component of the ML stability constant  $K^*$  (eq 32) is large with  $K^*/K \approx 8 \times 10^3$ , as we will comment on more in details below.

For the sake of comparison, we report in Figure 3 the (equilibrium) EDL potential distribution (Figure 3A), the (equilibrium) EDL field distribution (Figure 3B), and the M (Figure 3C) and ML (Figure 3D) concentration profiles at  $t = 93$  ms for  $c^\infty = 0.1, 1, 10$ , and 100 mM. As commented later, the time  $t = 93$  ms fits in the quasi-steady-state regime (nonequilibrium chemical regime). Besides the elements already discussed on the basis of Figure 2 (presence of maxima for the M and ML concentration profiles inside the particle reactive phase, M depletion feature, balance between M migration and

diffusion transports), parts A–D of Figure 3 make clear that (i) the increase of  $c_M$  and  $c_{ML}$  within the shell layer upon decrease of  $c^\infty$  is connected to the magnitude of the (Donnan) potential and that (ii) the depletion of M outside the shell is not only governed by diffusion process but also mediated for a large part by the EDL field distribution at  $r > a + d$ . In more detail, the position of the maxima in the M and ML concentration distributions is shifted deeper inside the shell when lowering  $c^\infty$ . This shift is directly correlated to that of the position where the EDL field starts to become significant within the shell layer ( $r < a + d$ ), recalling that deep inside the shell where the potential is constant ( $y(x \ll 1) = y^D$ ) the electric field is zero. In Figure 3A, the potential distributions based on the Debye–Hückel approximation (eq 34) are reported together with the rigorous numerical evaluations of the nonlinear Poisson–Boltzmann equation. Unsurprisingly, the merging between the two is excellent at large  $c^\infty$ , i.e., for low local potentials across the interphase, and becomes very poor upon decrease of  $c^\infty$  with a large overestimation of the exact numerical results by the analytical approach. For large  $c^\infty$ , the EDL potential profiles and EDL field are antisymmetric and symmetric with respect to the position ( $r = a + d$ ,  $y = y^D/2$ ) and the plane  $r = a + d$ , respectively. This is in agreement with a previous analysis.<sup>54</sup> Upon a decrease of  $c^\infty$ , these symmetry properties, though conserved with the analytical eq 34, gradually disappear, in line with the numerical study reported previously.<sup>52</sup>

In Figure 4, the time-evolution of the effective rate constant of colloidal complex formation,  $k_a^*(t)$  (eq 30), is reported for various electrolyte concentrations  $c^\infty$  under the conditions of Figures 2 and 3. For a given  $c^\infty$ , the characteristic features of the patterns  $k_a^*(t)/k_a$  are essentially those discussed by Duval et al. in their analysis of metal speciation dynamics in soft colloidal ligand suspensions with neglect of the interphasial EDL field.<sup>17</sup> Briefly, one identifies three distinct regimes. The first regime corresponds to the short time limit and reflects the dynamically developing M diffusion layer around the particle: the transient regime. The second regime follows the transitory establishment of M diffusion profile and it is characterized by a quasi-constant  $k_a^*/k_a$ : the quasi-steady-state regime. There, the diffusion flux at the edge of the EDL where the potential is zero, maintains its steady-state nature, that is

$$J_{\text{diff}}(t) = D_M \left. \frac{\partial c_M(r,t)}{\partial r} \right|_{a+R_0} \approx D_M \Delta c_M(t)/(a+d) \quad (39)$$

with  $\Delta c_M(t) = c_M(r=a+R_0,t) - c_M(r=a+R_0,t)$  and  $R_0$  is the radial position that defines the boundary between the EDL region and far-field domain (where  $y(r) = 0$ ).

For sufficiently long time  $t$ , the third and trivial regime (not reported here), already invoked when discussing the M and ML concentration profiles of Figures 2 and 3, is that where local M and ML concentrations are those dictated by Boltzmann statistics and eq 38 (local chemical equilibrium). On the basis of eqs 28, 30, 31, and 38 and Boltzmann statistics for M concentration profile, we directly obtain for  $t \rightarrow \infty$

$$\frac{k_a^*(t \rightarrow \infty)}{k_a} = \frac{K^*}{K} \quad (40)$$

which for  $y^D \rightarrow 0$  gives

$$k_a^*(t \rightarrow \infty) \rightarrow k_a \quad (41)$$

in agreement with ref 17. The limit provided by eq 41 means that, in the absence of the M and ML concentration gradient at the interphase core–shell/electrolyte (chemical equilibrium with



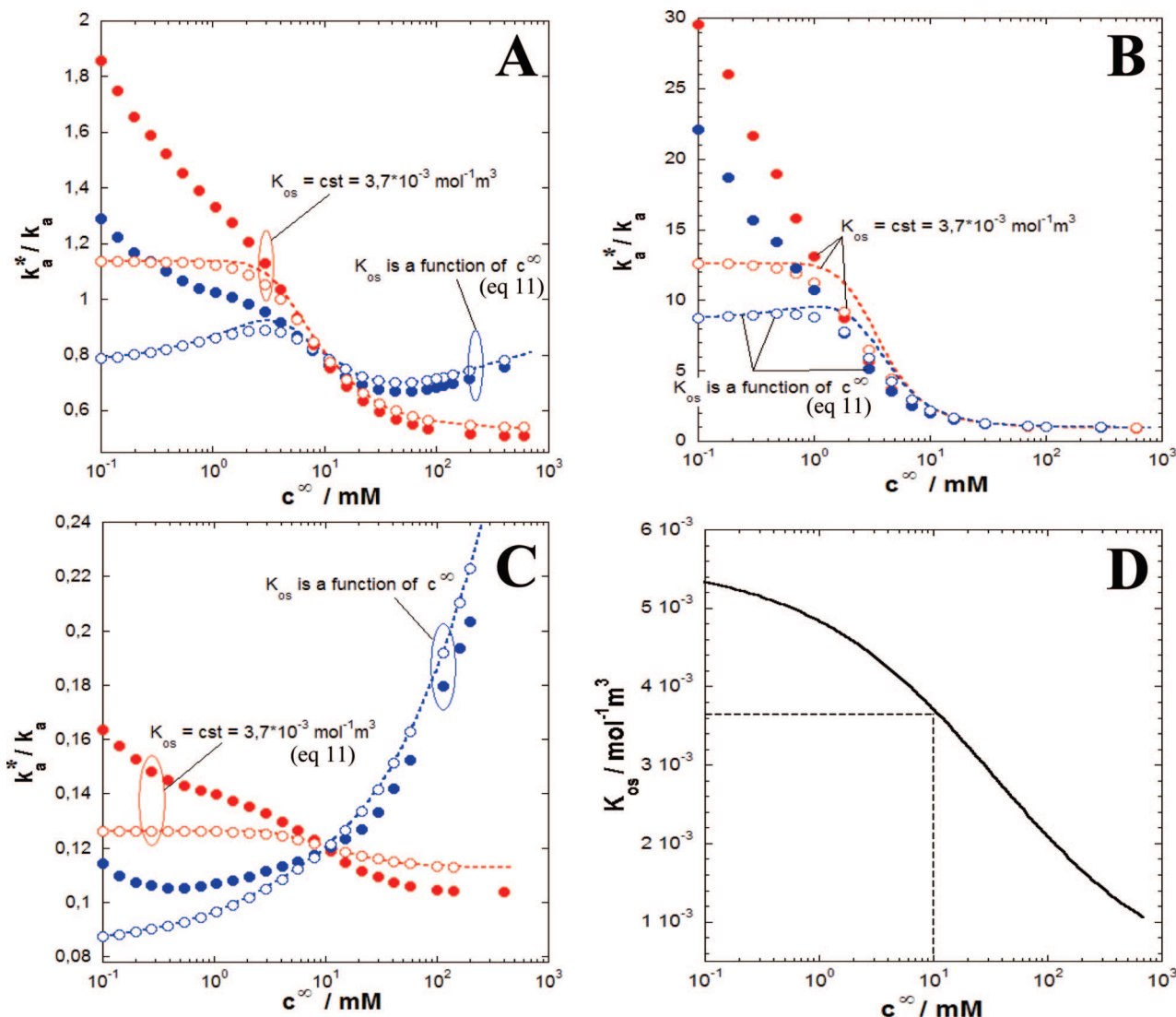


**Figure 5.** Ratio  $k_a^*/k_a$  in the time range that corresponds to the quasi-steady-state regime as a function of  $c^\infty$  for  $d = 100$  nm (A),  $d = 30$  nm (B), and  $d = 300$  nm (C). The red open/plain symbols and the red dotted lines denote calculations performed with  $K_{os} = 3.7 \times 10^{-3} \text{ mol}^{-1} \text{ m}^3 = K_{os}(c^\infty = 10 \text{ mM})$ , and the blue open/plain symbols and blue dotted lines pertain to computations carried out by taking eqs 10 and 11 into account (see motivations in the main text). In panels A, B, and C, plain symbols represent the rigorous evaluation of  $k_a^*/k_a$  (numerical analysis) and open symbols are the approximate estimations of  $k_a^*/k_a$  by means of eq 36 with  $y(r=a+d) \approx y(r=a)$  derived from solution of the rigorous nonlinear PB equation; dotted lines are approximate estimations of  $k_a^*/k_a$  by means of eq 36 with  $y(r=a+d) \approx y(r=a)$  derived from the solution of the linearized PB equation (eq 34). Other model parameters are as in Figure 2. (D) Dependence of  $K_{os}$  on  $c^\infty$  (eq 11) with  $z_{ML} = -2$  and  $a_{cc} = a_g = 5 \text{ \AA}$ .

$y^D \rightarrow 0$ ), the effective rate for ML formation in a solution of homogeneously distributed low-molar mass ligands is identical to that for ML formed with particle-confined ligands.

In line with the analysis in ref 17, the transient regime is marked by an initial increase of  $k_a^*(t)/k_a$  with time followed by a decrease for finally reaching quasi-steady-state value. The resulting maximum for  $k_a^*(t)/k_a$  is related to the increase of  $\rho_M^s(t)$  when increasing  $t$  (starting from  $k_a^*(t \rightarrow 0)/k_a \rightarrow 0$  in agreement with the boundaries in eqs 16–17) and the subsequent decrease of  $\rho_M^s(t)$  in relation with the gradual building up of the M diffusion layer at both sides of the very interface between shell layer and electrolyte solution (see parts A and C of Figure 2). At fixed time,  $k_a^*(t)/k_a$  increases with decreasing  $c^\infty$ . In light of the M and ML concentration profiles depicted in parts A and C of Figure 2, this increase is intrinsically related to the significant Donnan partitioning of M at the colloidal ligand interphase upon decrease of  $c^\infty$  (Figure 3A), which leads to larger  $\rho_M^s(t)$ . As previously discussed, the time required for reaching local chemical equilibrium (eq 38) increases with decreasing  $c^\infty$ . Figure 4 illustrates that the time necessary for the establishment

of the nonequilibrium chemical regime (quasi-steady-state) is also increasing when lowering  $c^\infty$ , in relation with the corresponding increase of the magnitude of the maximum mentioned above.

**3.2. Impact of Colloidal Ligand Particle Dimensions on the Ionic-Strength Dependence of  $K^*$  and of  $k_a^*/k_a$  in the Quasi-Steady-State Regime.** The finite rates of association of colloidal metal complexes are accessible, together with the thermodynamic complex stability constant by, e.g., steady-state deposition potential stripping chronopotentiometry (SSCP) experiment.<sup>14</sup> The dynamic parameter  $k_a^*$  in the quasi-steady-state regime is displayed in Figure 5A as a function of ionic strength for a soft particle devoid of core (porous particle of radius  $d = 100$  nm). To facilitate the understanding of the interrelationships between EDL potential/field profiles, M/ML concentration polarizations, and  $k_a^*/k_a$ , the simulations are reported under the conditions that match those adopted in Figures 2–4 (see captions for further details). Also, we show the dependence of  $k_a^*/k_a$  on  $c^\infty$  when  $K_{os}$  is evaluated according to eq 11. In Figure 5B,C, the dynamic features of metal



speciation are further depicted as a function of  $c^\infty$  for porous particles of radius  $d = 30$  nm and  $d = 300$  nm, respectively. In line with recommendations given in refs 14 and 17, the comparison between the dynamic features of metal speciation by colloidal ligands of different radii is rendered possible by keeping the smeared-out ligand concentration  $\rho_L^V$  (eq 29) constant upon changing  $c_p$  (or equivalently  $V_c$ ) via imposing  $r_c = \theta(a + d)$  with  $\theta$  a scalar adjusted to comply eq 29 with  $\rho_L^V = \text{constant}$  (it is recalled that  $\rho_L^V$  satisfies the equality  $\rho_L^V/c_L^* = V_s/V_c$ <sup>17</sup>). Besides,  $\theta$  systematically verifies the condition  $\theta \gg 1$ , which warrants fast achievement of the quasi steady state.<sup>9,14,17</sup>

From parts A–C of Figure 5, it is noted that at large  $c^\infty$  and for  $K_{os} = \text{constant} = 3.7 \times 10^{-3} \text{ mol}^{-1} \text{ m}^3$  (red curves),  $k_a^*$  (as obtained from eq 30) tends to a constant value, which is expected because  $y(r) \rightarrow 0$  for  $c^\infty \rightarrow \infty$ . More interestingly, at large  $c^\infty$ ,  $k_a^*$  may significantly deviate from  $k_a$  upon an increase of the porous particle radius. As extensively discussed in ref 17, this discrepancy is due to the significant contribution of the M diffusion transport within and outside the shell in determining the overall colloidal complex formation rate constant. Under conditions where  $k_a^*/k_a \ll 1$  (panel C), metal speciation is predominantly rate-limited by diffusive transport of M to/from the shell that contains the binding sites L. For  $k_a^*/k_a \approx 1$  (panel B), this is the kinetics of interconversion of M into ML (i.e., the constants  $k_{a,d}$ ) that governs the overall speciation process: the nonequilibrium regime governed by chemical kinetics. For intermediate values of  $k_a^*/k_a$  (panel A), the kinetic determinants of eq 9 and the M diffusion transport concomitantly come into play. Taking the behavior at  $c^\infty \rightarrow \infty$  as a reference in the following,  $k_a^*/k_a$  evaluated from the rigorous numerical analysis of the governing M/ML transport equations (adopting  $K_{os} = \text{constant} = 3.7 \times 10^{-3} \text{ mol}^{-1} \text{ m}^3$ ), gradually increases when decreasing  $c^\infty$ . The smaller the size of the ligand particle the larger is this increase with respect to  $k_a^*/k_a$  values evaluated at  $c^\infty \rightarrow \infty$ . To understand this, it is recalled that upon a decrease of  $c^\infty$  the EDL field and potential distribution interfere to some important extent with the M diffusion process in determining the M/ML concentration polarizations across the interphase core–shell/electrolyte. Conductive transport of M in the EDL region and diffusion of M as a result of difference between M electrochemical potentials in shell and bulk solution act indeed in opposite directions: M migration in the EDL field region tends to counterbalance via electrostatic partitioning the M concentration gradients built up by diffusion (see parts A and C of Figure 2). The balance between the interphasial M fluxes associated with these two transport modes is exactly met at chemical equilibrium (see Supporting Information). As a result, the larger the contribution of diffusion transport in rate-limiting metal speciation (i.e., the larger the ligand particle size), the smaller the impact of the counteracting electrostatic EDL field in determining the magnitude of  $k_a^*/k_a$  in the quasi-steady-state regime. In line with this, for a given particle size, the increase of  $k_a^*/k_a$  with decreasing  $c^\infty$  is related to the enhancement of local M concentration within the shell due to electrostatic partitioning (see discussion of Figure 4). The latter diminishes the diffusion-derived component of the overall complexation rate, thereby rendering the process more kinetically limited (increase of  $k_a^*$ ) than it is for  $c^\infty \rightarrow \infty$ .

In parts A–C of Figure 5, we report, for the sake of comparison, the dependence of  $k_a^*/k_a$  with  $c^\infty$  as obtained from the approximate analytical expression given by eq 36 and for  $K_{os} = \text{constant} = 3.7 \times 10^{-3} \text{ mol}^{-1} \text{ m}^3$ . For that purpose, the required value for the potential  $y(r=a+d)$  in eq 36 is assimilated to  $y(r=a)$  as obtained from the rigorous solution of the nonlinear

Poisson–Boltzmann (PB) equation (eqs 23–26) and from the solution of the linearized PB equation (Debye–Hückel formulation, eq 34). The assimilation  $y(r=a+d) \approx y(r=a)$  constitutes one of the approximations underlying the validity of eq 36 that tacitly presumes that a constant surface or Donnan potential (depending on  $\kappa d$  value, see comment below eq 36) may be attributed to the entire shell layer. In cases where  $y(r=a)$  is evaluated from nonlinear and linearized PB equations, the  $k_a^*/k_a$  vs  $c^\infty$  plots exhibit very similar “sigmoid” patterns: starting from  $c^\infty \rightarrow \infty$  where  $k_a^*/k_a$  is constant (the colloidal charge is completely screened),  $k_a^*/k_a$  sequentially increases upon decreasing  $c^\infty$  before reaching an asymptotic plateau to some lower value of  $c^\infty$ . The gradual increase of  $k_a^*/k_a$  with decreasing  $c^\infty$  corresponds to M electrostatic partitioning across the interphase, as argued for the rigorous numerical results. The presence of the plateau revealed by the analytical expression (36), is explained by realizing that in the limit of very low  $c^\infty$  (i.e., very large  $y(r=a)$  in magnitude), eq 36 may be rewritten as

$$k_a^*(c^\infty \rightarrow 0) \approx \frac{4\pi(a+d)D_M c_p}{\rho_L^V} \quad (42)$$

which is independent of  $y(r=a)$  or, for that matter,  $c^\infty$ . Of course, depending on the very value of  $k_a$ , the critical concentration of indifferent electrolyte in agreement with eq 42 will be different: the lower  $k_a$ , the lower is this critical concentration. Inspection of parts A–C of Figure 5 indicates that eq 36 used in conjunction with the nonlinear and linearized PB equations provides, for a given particle size, identical predictions for  $k_a^*/k_a$  at sufficiently low  $c^\infty$ , in agreement with eq 42, and at sufficiently large  $c^\infty$ . In the limit of large  $c^\infty$ , the potential  $y(r=a)$  is indeed so low that treatment of the nonlinear PB equation on the basis of Debye–Hückel approximation is justified (see Figure 3A). In the intermediate  $c^\infty$  range just preceding that where the aforementioned plateau is reached, the discrepancies between  $k_a^*/k_a$  estimations based on eq 36 with the linearized and rigorous solutions of the PB equation increase with decreasing particle size. Indeed, for particles of radius that low that kinetics predominantly governs the magnitude of  $k_a^*$ , eq 36 approximates, in this  $c^\infty$  range, to

$$k_a^*/k_a \approx \exp(-z_M y(r=a+d)/z) \quad (43)$$

Consequently, discrepancies between values of  $k_a^*/k_a$  evaluated from nonlinear and linearized PB equations directly reflect the overestimation of  $y(r=a)$  (assimilated to  $y(r=a+d)$ ) from Debye–Hückel treatment of electrostatics as compared to the rigorous solution obtained from nonlinear PB equation (Figure 3A). In addition, the larger the particle size, the more the quantity  $[k_a \exp(-z_M y(r=a+d)/z) \rho_L^V] / [4\pi(a+d)D_M c_p]$  in eq 36 exceeds 1 (we recall that  $\rho_L^V/c_p = V_s c_L^* \sim d^3$  for  $a \rightarrow 0$ ), the larger the concentration  $c^\infty$  where the plateau is reached (eq 42), and the smaller the dependence of  $k_a^*/k_a$  on  $c^\infty$ , in agreement with results of parts A–C of Figure 5.

Qualitatively, the approximate eq 36 supports the numerically evaluated  $k_a^*/k_a$  in the sense that it correctly underpins the extent to which  $k_a^*/k_a$  depends on  $c^\infty$ : the larger the particle size, the lesser pronounced is this dependence because the larger the rate limitation of speciation by M diffusion to/from the shell. Quantitatively, however, small and major differences are found between analytically and numerically estimated  $k_a^*/k_a$  at sufficiently large and low values of  $c^\infty$ , respectively. For large  $c^\infty$ , the analytical eq 36 overestimates, within a few percent error, the exact numerical results. This discrepancy was already largely discussed in ref 17 and is assigned to the neglect in eq 36 of

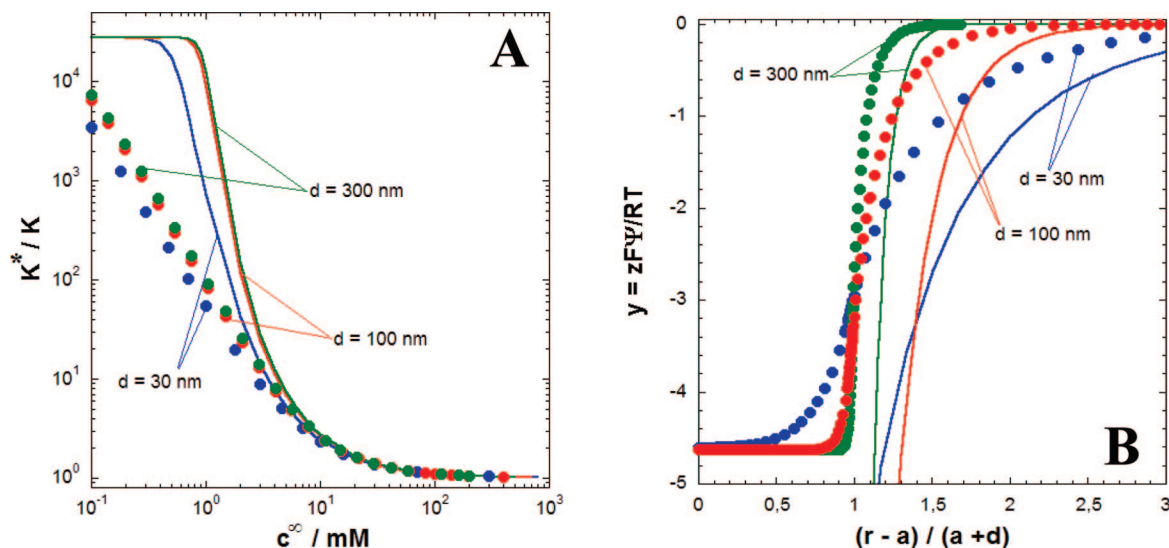


**Figure 6.** Dependence of the ML stability constant  $K^*$  on  $c^\infty$  (A) and the dimensionless EDL potential distribution at 0.1 mM (B) for porous particles of radii 30, 100, and 300 nm (indicated). Symbols in part A are predictions based on eq 32 and the nonlinear PB equation. Plain lines in part A are predictions based on eq 32 and the linearized PB equation. Symbols in part B are predictions based on the nonlinear PB equation. Plain lines in part B are predictions based on eq 34. Other model parameters are as in Figure 2.

the M and ML concentration polarizations within the shell layer: the larger the latter, the poorer the approximation of constant M/ML concentration in the shell layer and the lesser accurate eq 36 (parts A–C of Figure 5). More seriously, eq 36 significantly underestimates the exact  $k_a^*/k_a$  for sufficiently low  $c^\infty$ : though eq 36 leads to a plateau in the  $k_a^*/k_a$  vs  $c^\infty$  plot (eq 42), the numerically evaluated ratio  $k_a^*/k_a$  keeps on increasing with decreasing  $c^\infty$ . This fundamental difference is due to the neglect of the field distribution within and outside the shell in deriving eq 36. At low  $c^\infty$ , the spatial regions where the EDL field magnitude deviates from zero are more extended than at larger  $c^\infty$  (Figure 3B). Doing so, the coupling between M electromigration in the interphasial field inside and outside the particle, and M diffusion transport is entirely overlooked in eq 36. To put it in a nutshell, we state that eq 36 is acceptable as long as the extension of the electric double layer inside and outside the shell is small or moderate as compared to the thickness of the shell layer, that is, for  $\kappa_m d \gg 1$ . When the latter condition is not satisfied, accurate account of the EDL field necessarily requires taking into account the nonlinear terms reflecting the coupling between electrostatics and concentration polarizations (inside and outside the shell) in the governing transport equation for free metal M species (eqs 14 and 15).

Let us now comment on the effect of  $c^\infty$  on  $k_a^*/k_a$  when the impact of electrostatics on the local kinetic rate constant  $k_a$  (eqs 10 and 11) compounds that previously discussed and associated to the action of the only colloidal EDL field developing within and outside the particle (blue curves, Figure 5). Starting from  $c^\infty \rightarrow \infty$ , numerically evaluated  $k_a^*/k_a$  then sequentially decrease and, for lower  $c^\infty$ , increase upon further reduction of  $c^\infty$ . For sufficiently large  $c^\infty$  where the effect of the colloidal EDL on  $k_a^*/k_a$  is marginal, the dependence of  $K_{os}$  on  $c^\infty$  (eqs 10 and 11, Figure 5D) leads to increasing  $k_a$  upon a decrease of  $c^\infty$ . As a result, the complexation process becomes increasingly diffusion limited because the M–ML interconversion kinetics becomes faster. This effectively leads to decreasing  $k_a^*/k_a$ . This decrease is the most important for the system where diffusion predominantly limits the speciation process, i.e., for large particle size, Figure 5C. On the contrary, it is reduced (Figure 5A) and even absent (Figure 5B) for particles of smaller size where local ML complex formation kinetics controls significantly and exclusively

the overall speciation rate. For sufficiently low electrolyte concentrations, the impact of the colloidal EDL field on the ratio  $k_a^*/k_a$  overrules that related to the dependence of  $K_{os}$  on  $c^\infty$  previously discussed. In turn,  $k_a^*/k_a$  increases upon further decrease of  $c^\infty$  for the same reasons as those invoked for explaining the action of the (only) EDL field at constant  $K_{os}$ . For a given  $c^\infty < 10$  mM ( $c^\infty > 10$  mM, respectively), eq 30 (numerical computation) and the analytical eq 36 with taking into account eq 11, lead to lower (larger, respectively)  $k_a^*/k_a$  values as compared to those obtained with  $K_{os} = 3.7 \times 10^{-3} \text{ mol}^{-1} \text{ m}^3 = K_{os}(c^\infty = 10 \text{ mM})$ . This is easily explained by arguing that the inequality  $K_{os}(c^\infty < 10 \text{ mM}) > K_{os}(c^\infty = 10 \text{ mM})$  ( $K_{os}(c^\infty > 10 \text{ mM}) < K_{os}(c^\infty = 10 \text{ mM})$ , respectively) (see Figure 5D) basically means that the speciation process is more critically diffusion limited (kinetically controlled, respectively) for  $c^\infty < 10$  mM ( $c^\infty > 10$  mM, respectively) than for  $c^\infty = 10$  mM. Finally, we mention that the respective positioning of the  $k_a^*/k_a$  vs  $c^\infty$  plots obtained from the analytical eq 36 (within linear and nonlinear formulations of the PB equation) and from the numerical analysis (eq 30), both used with  $k_a$  computed on the basis of eq 11, is essentially the same as that commented above for analyzing situations where the  $c^\infty$  dependence of  $K_{os}$  was ignored. In addition, at sufficiently low  $c^\infty$ , one easily captures the decrease of  $k_a^*/k_a$  with decreasing  $c^\infty$ , as predicted by analytical eq 36 used in conjunction with eqs 10 and 11: for such low  $c^\infty$ ,  $k_a^*$  is independent of the colloidal EDL field or  $c^\infty$  (eq 42), whereas  $k_a$  (or equivalently  $K_{os}$ ) increases with lowering ionic strength (Figure 5D).

In Figure 6, the dependence of the ML complex stability constant  $K^*$  (eq 32) on  $c^\infty$  is displayed for porous ligand particles of radius  $d = 30$ , 100, and 300 nm. For the sake of comparison, estimations based on Debye–Hückel treatment of the PB equation (eq 34) are also reported. Upon a decrease of  $c^\infty$ , i.e., for increasing local EDL potentials  $|y(r)|$  (Figure 3A),  $K^*$  increases and deviates significantly from the intrinsic chemical contribution  $K$ , as a result of the correction brought about by interphasial M electrostatic partitioning. For a given particle size and sufficiently large  $c^\infty$  (i.e., sufficiently low  $|y(r)|$ ), merging is reached between predictions based on the rigorous PB equation and the approximate Debye–Hückel PB formulation, as expected. For homogeneous intraparticle ligand

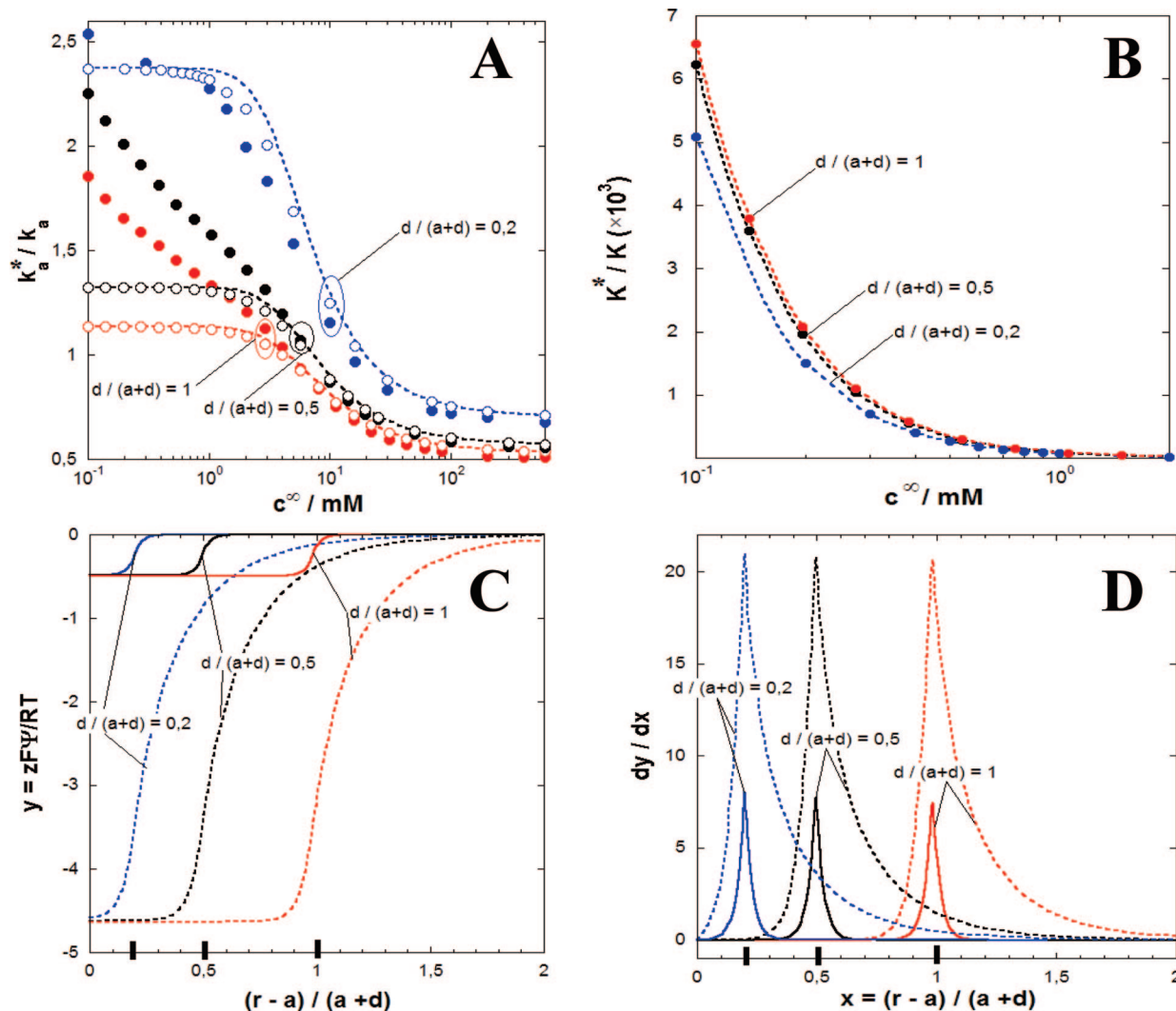


**Figure 7.** (A) Ratio  $k_a^*/k_a$  in the time range that corresponds to the quasi-steady-state regime as a function of  $c^\infty$  for particle radius  $a + d = 100$  nm and various shell thickness (indicated). The results are reported for  $K_{os} = 3.7 \times 10^{-3} \text{ mol}^{-1} \text{ m}^3 = K_{os}(c^\infty = 10 \text{ mM})$ . Plain symbols are the rigorous evaluation of  $k_a^*/k_a$  (numerical analysis), open symbols are approximate estimations of  $k_a^*/k_a$  by means of eq 36 with  $y(r=a+d) \approx y(r=a)$  derived from solution of the rigorous nonlinear PB equation, and dotted lines are the approximate estimations of  $k_a^*/k_a$  by means of eq 36 with  $y(r=a+d) \approx y(r=a)$  derived from the solution of the linearized PB equation (eq 34). Other model parameters are as in Figure 2 with adjusted  $r_c$  to comply with the condition  $\rho_L^V = 3.7 \times 10^{-4} \text{ mol m}^{-3}$ . (B) Dependence of the ML stability constant  $K^*$  (eq 32 used in conjunction with the nonlinear PB equation) on  $c^\infty$  for particle radius  $a + d = 100$  nm and various shell thickness (indicated). Dotted lines are only guides to the eye. (C) and (D) Distribution of the dimensionless EDL potential and EDL field based on the nonlinear PB equation at 10 mM (plain lines) and 0.1 mM (dotted lines) for particle radius  $a + d = 100$  nm and various shell thickness (indicated). The boundaries between shell layer and outer electrolyte medium are indicated on the abscissa axis. Other model parameters are as in part A.

distribution, considering  $y(a \leq r \leq a+d) \approx y^D$  and  $y(r \geq a+d) \approx 0$ , we show in the limit  $|y^D| \gg 1$  (reached for sufficiently low  $c^\infty$ , see eq 37)

$$K^*/K(c^\infty \rightarrow 0) \approx V_c/V_s \quad (44)$$

which is in line with the results of Figure 6. Upon a decrease of the ionic strength, the limit given by eq 44 is reached for lower  $c^\infty$  within the framework of the nonlinear PB equation than within Debye–Hückel approach for the electrostatics. This is so because the latter overestimates the local EDL potentials, as illustrated in Figure 6B. Finally, at a given  $c^\infty$ , subtle differences are observed for  $K^*$  as computed for porous ligand particles of various radii. These differences are attributed to variations in the spatial integrals of the corresponding potential distributions (see eq 32) within and outside the shell, as pictured in Figure 6B. In detail, the larger  $\kappa d$  at given  $c^\infty$  (the more acceptable the relationships  $y(a \leq r \leq a+d) \approx y^D$  and  $y(r \geq a+d)$

$\approx 0$ ), the larger the spatial integral of the potential profile over the shell layer and the larger  $K^*$ .

**3.3. Impact of the Core to Shell Ratio on the Ionic-Strength Dependence of  $k_a^*/k_a$  and  $K^*$ .** In parts A and B of Figure 7, we report the dependence of  $k_a^*/k_a$  and  $K^*$  on  $c^\infty$  for particles of constant overall size  $a + d = 100$  nm but defined by various core to shell ratios as expressed by  $d/(a + d) = 0.2, 0.5$ , and 1. As in Figures 5 and 6, results are given for a constant  $\rho_L^V$  via adjustment of  $r_c$ . For the sake of conciseness, the analysis is carried out here by focusing solely on the impact of the colloidal field/potential, i.e., for  $K_{os} = 3.7 \times 10^{-3} \text{ mol}^{-1} \text{ m}^3 = K_{os}(c^\infty = 10 \text{ mM})$ , thus ignoring the  $c^\infty$  dependence of  $K_{os}$  given by eq 11. Account of eq 11 leads to changes in the  $c^\infty$  dependence of  $k_a^*/k_a$  along the lines extensively discussed in Figure 5 (not shown).

For  $c^\infty \rightarrow \infty$ , the charge carried by the colloidal ligand particle is completely screened, the local potential and local field across



the interphase both go to zero and the numerically evaluated ratio  $k_a^*/k_a$  tends to a constant value, as expected. In agreement with conclusion of the previous section,  $k_a^*/k_a$  increases upon a decrease of  $c^\infty$  as a result of the EDL field that counteracts the interphasial M diffusion process. For a given indifferent electrolyte concentration  $c^\infty$ , the lower the ratio  $d/(a+d)$ , i.e., the smaller the shell layer thickness, the more kinetically controlled the metal speciation or, stated differently, the larger  $k_a^*/k_a$ . Also, the lower  $d/(a+d)$ , the larger the increase of  $k_a^*/k_a$  with respect to the value obtained at  $c^\infty \rightarrow \infty$ . These two last features basically underline that modulation of the particle shell thickness at constant overall size results in variations of the dynamic parameter  $k_a^*/k_a$  as a function of  $c^\infty$ , which are qualitatively in line with those discussed in Figure 5 where the particle size is varied at constant core to shell ratio. In more detail, the increase of  $k_a^*/k_a$  at a given  $c^\infty$  for decreasing shell layer thickness (or increasing core radius) originates from the M/ML local interconversion kinetics that affect and possibly fully control metal speciation in colloidal ligand suspensions. Said differently, the diffusive flux around the particle no longer rate limits the process upon diminishing the M/ML concentration polarizations within the shell layer. This was already found<sup>17</sup> in the limit of neglect of EDL electrostatics, i.e., at  $c^\infty \rightarrow \infty$ . In addition, the increase of  $k_a^*/k_a$  with decreasing  $c^\infty$  is most significant for ligand particles where kinetics significantly or predominantly rate-limits M speciation process, i.e., for particles with thin soft surface layer thickness (small values of  $d/(a+d)$ ). Such particle geometries rapidly fall within the so-called thin electric double layer limit (low  $\kappa d$  values) upon a decrease of  $c^\infty$ : the EDL potential and field profiles then exhibit the most remarkable changes within the shell layer (parts C and D of Figure 7), with the picture of Donnan partitioning (at the basis of eq 36) that becomes necessarily incorrect for sufficiently low  $\kappa d$ . The comparison of the rigorous numerical results with those estimated from the approximate eq 36 used in conjunction with the analytical and numerical solutions of the PB equation is entirely analogous to that extensively commented in Figure 5. To conclude this section, Figure 7B illustrates that the stability constant  $K^*$  depends on the core to shell ratio because the latter intrinsically governs the potential and field distributions across the interphase (parts C and D of Figure 7). At fixed  $c^\infty$ , the lower  $\kappa d$  (i.e., the smaller the shell thickness), the lower the local EDL potential and consequently the lower the electrostatic correction to the intrinsic chemical component  $K$ .

**3.4. Impact of Intraparticle Ligand Distribution on  $k_a^*/k_a$  and  $K^*$ .** As a final step in our analysis of the impact of electrostatics on metal speciation dynamics in suspension of soft particles, we explicitly investigate the case where ligand distribution within the shell is diffuse ( $\alpha/d > 0$ ), i.e., gradually decreasing from bulk values in the heart of the shell component of the particle to zero at the very interface formed with the outer electrolytic medium (Figure 8A). Starting from the situation of homogeneous soft interphase ( $\alpha/d \rightarrow 0$ ), increasing  $\alpha/d$  leads to increasing and decreasing the local ligand concentration in the vicinity of the particle core and in the outer shell layer, respectively, in agreement with eqs 4 and 5. The condition of constant total amount of ligand sites throughout the shell layer (imposed by eq 5) leads, for sufficiently large values of  $\alpha/d$ , to a ligand distribution profile that becomes independent of the interphasial diffuseness parameter  $\alpha/d$  (Figure 8A). Note that the area under the curves described by the function  $4\pi r^2 c_L(r)/c_L^*$  are identical and equal to  $V_s$ . The effect of the position-dependent ligand distribution on the EDL potential is displayed in Figure 8B for selected values of  $\alpha/d$ . In line with the ligand

profile previously commented, upon an increase of  $\alpha/d$ , the local EDL potential increases (in magnitude) in the spatial region where one basically injects charges or ligand sites (close to the particle core), and conversely, it decreases in the interfacial region around the position  $r = a + d$  where charges are depleted. When  $\alpha/d$  is increased, the nature of the ligand distribution gradually renders inappropriate the approximation of Donnan potential where the potential within the soft surface layer is considered as constant. The effect of the interphasial ligand profile details on the EDL field distribution is reported in Figure 8C. Namely, deviations from homogeneous repartition of ligands within the shell layer result in decreasing maxima for the EDL field as well as a shift of their location toward the heart of the particle. As for the potentials, the EDL field locally increases (decreases, respectively) in the regions where  $c_L(r)$  is enhanced (decreased, respectively) with increasing  $\alpha/d$ .

On the basis of these modifications of the EDL potential and field profiles as related to the diffuseness extent of the interphase, we may now comment on the  $c^\infty$  dependence of  $k_a^*/k_a$  (in the quasi-steady-state regime) as a function of  $\alpha/d$  (Figure 9A) starting with  $K_{os} = K_{os}(c^\infty=10 \text{ mM})$ . In agreement with the results of Figures 5–7,  $k_a^*/k_a$  increases with decreasing  $c^\infty$  at fixed  $\alpha/d$  because M electromigration in the EDL region effectively leads to metal speciation that is more kinetically controlled. However, increasing  $\alpha/d$  at fixed  $c^\infty$  results in a decrease of  $k_a^*/k_a$  before it levels off at large  $\alpha/d$ . This leveling off is easily explained by recalling that the concentration ligand profile and therewith the EDL field and potential distributions becomes independent of the interphasial diffuseness for sufficiently large values of  $\alpha/d$ . The decrease of  $k_a^*/k_a$  with increasing  $\alpha/d$  is the direct consequence of the associated EDL field and potential variations in the zones where ligand concentration is either enhanced or depleted (Figure 8C). These variations result in M electrostatic partitioning that is greatly hindered in the outer shell layer whereas the increase of local potential in the vicinity of the core leads therein to a significant increase of the free M concentration, as illustrated in Figure 9C where M concentration profiles are given for selected values of  $\alpha/d$  at 0.1 mM ionic strength. The overall picture is that the decrease of the EDL field just outside the shell layer upon increase of  $\alpha/d$  favors the building of a concentration gradient of free M species by diffusion from bulk solution toward the particle. Therefore, EDL electrostatics counteracts to a lesser extent the diffusion transport, which effectively leads to a decrease of the overall speciation rate constant  $k_a^*$  when increasing  $\alpha/d$ . This decrease of  $k_a^*$  is the most significant at low electrolyte concentrations, where the EDL field and potential are large, and reduces in magnitude or even disappears at sufficiently large  $c^\infty$  (under the conditions of Figure 9, at  $c^\infty \sim 10 \text{ mM}$ ). When the impact of  $\alpha/d$  on  $k_a^*/k_a$  is analyzed at 0.1 and 1 mM by taking into account the  $c^\infty$  dependence of  $k_a$  as expressed by eqs 10 and 11, the curves are basically shifted downward in agreement with the results of Figure 5A obtained for  $\alpha/d \rightarrow 0$ . Coming back to the concentration profiles of M as depicted in Figure 9C and those of local ML complex reported in Figure 9D, it is noteworthy that they are reminiscent of that of the local ligand concentration within the shell layer (Figure 8A) or, equivalently, of those for the EDL field and potential profiles (parts B and C of Figure 8).

Finally, for the sake of completeness, Figure 9B shows that the thermodynamic ML stability constant  $K^*$  is also depending, via the interphasial electrostatic potential distribution, on the ligand concentration profile within the soft shell layer. More explicitly, the increase of the local potential close to the core



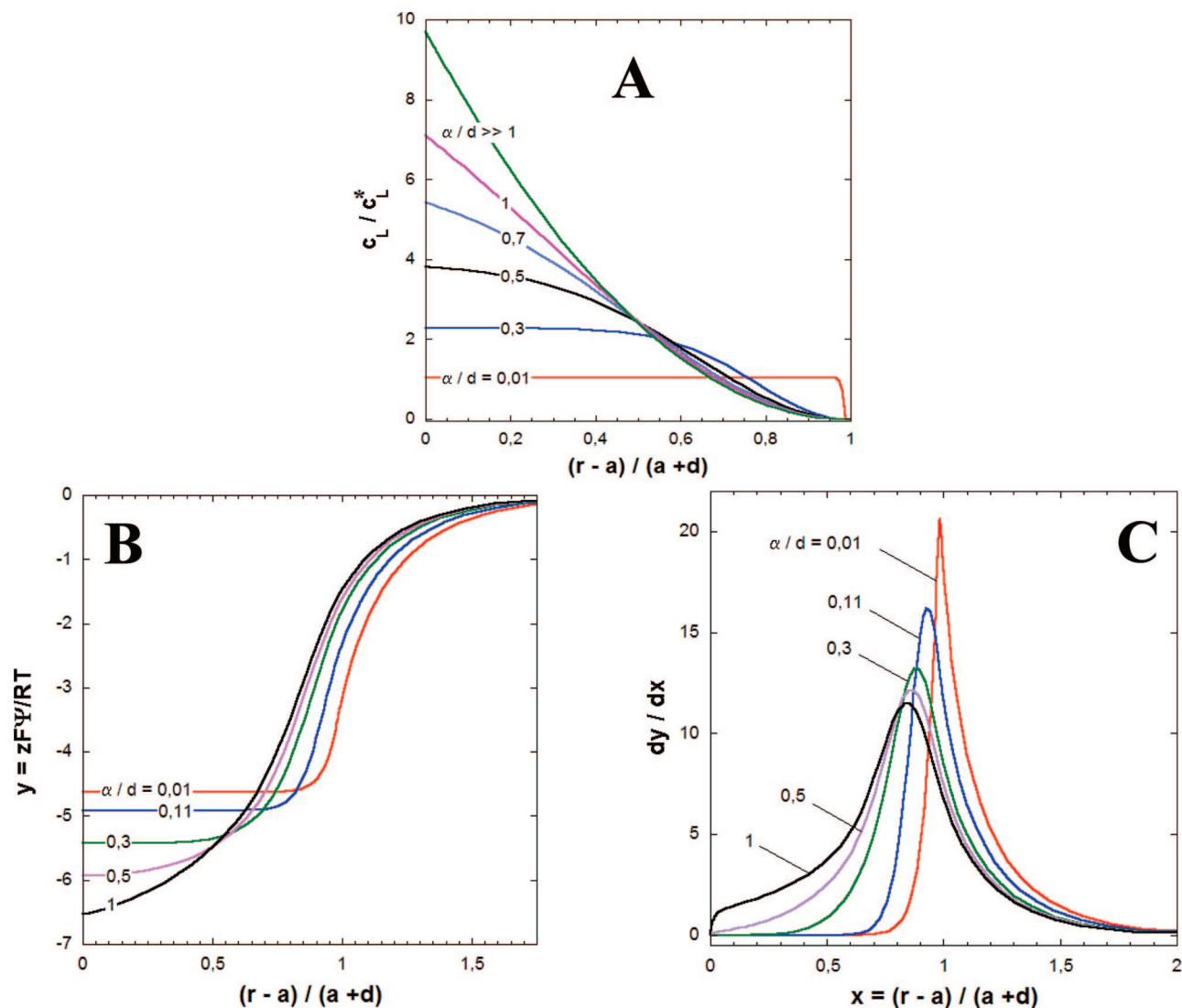


**Figure 8.** (A) Distribution of ligand concentration within the shell layer for various  $\alpha/d$  of the interphase core/shell/electrolyte (indicated). Distributions of the electric double layer potential (panel B) and field (panel C) at 0.1 mM and various  $\alpha/d$  (calculation based on the nonlinear PB equation). Other model parameters are as in Figure 2.

surface as a result of increasing  $\alpha/d$ , leads to increasing values of  $K^*$ . Doing so, increasing  $\alpha/d$  at fixed  $c^\infty$  or decreasing  $c^\infty$  at fixed  $\alpha/d$  yields a significant electrostatic correction to be applied to  $K$  as compared to the situations at  $\alpha/d \rightarrow 0$  or  $c^\infty \rightarrow 0$ , respectively.

#### 4. Conclusions: Consequences for the Dynamic Evaluation of ML Colloidal Complex

To conclude our analysis, we briefly underpin some consequences of the findings reported here on the dynamic evaluation of ML colloidal complex systems. As extensively discussed previously,<sup>14,17</sup> the dynamic criterion for colloidal metal complex resulting from the interaction between M and particle-confined ligands should be evaluated by replacing the complex association–dissociation rate constants  $k_{a,d}$ , valid for homogeneous ligand solution, by their colloidal equivalents  $k_{a,d}^*$ . For dynamic ML colloidal complex, the effective rates  $k_{a,d}^*$  are fast on the experimental time scale  $t$ , thus yielding

$$k_d^* t, k_a^* \rho_L^V t \gg 1 \quad (45)$$

Provided eq 45 is satisfied, thermodynamic equilibrium between M and ML is fully maintained in the bulk volume.

The other limit is given by  $k_d^*, k_a^* \rho_L^V t \ll 1$ , which pertains to static or inert ML complexes. In the situation of practical interest where there is a consuming interface, e.g., an electrode or a micro-organism acting as a sink for the free metal species, the overall M flux from/toward the consuming interface is governed by the interplay between diffusions of M and (colloidal) ML and M–ML interconversion kinetics, as subsumed in the rate constants  $k_{a,d}^*$ . The lability criterion is a measure of the contribution of the colloidal metal complex to the overall metal flux from/toward the consuming interface. It is defined by the ratio  $L^* = J_{\text{kin}}^*/J_{\text{diff}}^*$ , where  $J_{\text{diff}}^*$  and  $J_{\text{kin}}^*$  are the purely ML diffusional flux and the flux resulting from net dissociation of ML, respectively. We then classically define the two limits for dynamic systems, those controlled by diffusion (labile ML colloidal complexes,  $L^* \gg 1$ ) and those rate-limited by kinetics (nonlabile ML colloidal complexes,  $L^* \ll 1$ ).

On the basis of the results discussed in this study, we state that the dynamic and (electrochemical) lability criteria (the expressions of which are determined to some extent by the thermodynamic complex stability constant  $K^*$ , eq 32<sup>6</sup>) for

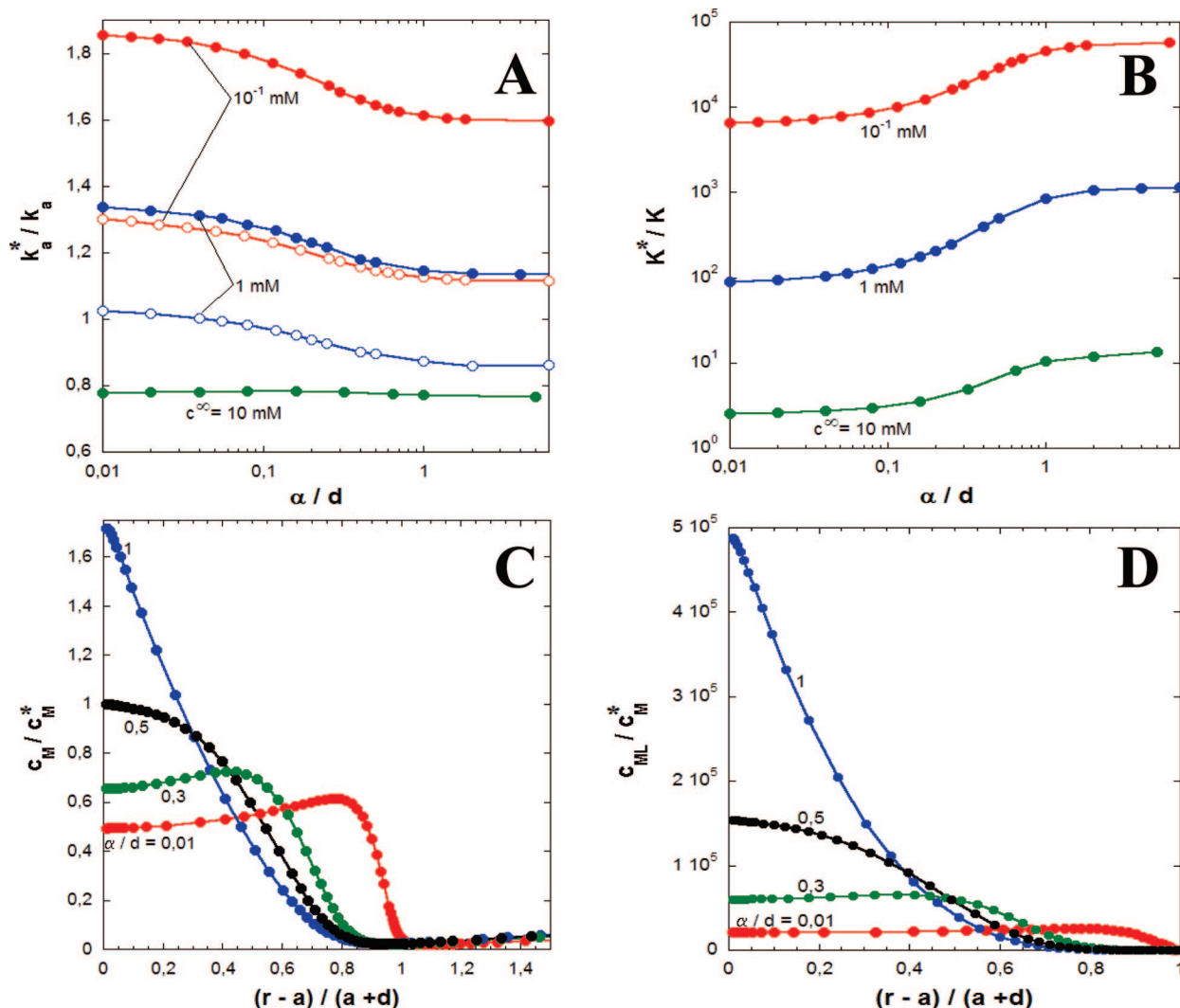


**Figure 9.** (A) Ratio of  $k_a^*/k_a$  in the time range that corresponds to the quasi-steady-state regime as a function of  $\alpha/d$  for 0.1, 1, and 10 mM electrolyte concentration. Plain symbols refer to numerical computations with  $K_{os} = 3.7 \times 10^{-3} \text{ mol}^{-1} \text{ m}^3 = K_{os}(c^\infty = 10 \text{ mM})$ , and open symbols pertain to those carried out by taking eq 11 into account. Other model parameters are as in Figure 2. (B) Dependence of the ML stability constant  $K^*$  (eq 32 used in conjunction with the nonlinear PB equation) on  $\alpha/d$  for 0.1, 1, and 10 mM electrolyte concentration. Model parameters are as in panel A. (C) and (D) Concentration profiles for M (panel C) and ML (panel D) at  $t = 0.17 \text{ s}$  (quasi-steady-state regime) and 0.1 mM electrolyte concentration for various  $\alpha/d$  (indicated). Other model parameters are as in panel A.

colloidal metal complex systems will be strongly depending not only on the particle size, as extensively discussed earlier,<sup>6,14,17</sup> but also on

(I) the background electrolyte concentration that leads to changes in the interphasial EDL potential and field distribution;

(II) the solution pH or, more generally, the concentration of charge determining ions, which affects the ligand (and charge) concentration within the shell, thereby inducing modifications of the electrostatic characteristics of the interphase core/shell/electrolyte; and

(III) the very spatial distribution of ligands within the shell layer, which in turn impacts the EDL composition.

More often than not, effects I–III on metal speciation dynamics in soft colloidal ligand suspensions are intrinsically coupled. The (titrable) charge carried by soft particles depends on the local electrostatic potential within the shell layer as concomitantly determined by the salt amount in the medium and solution pH (see eq 8). Also, the structural properties of microgel ligand particles<sup>19</sup> or soft bioparticles like bacteria<sup>23</sup> are modulated upon variations of the interphasial electrostatics via change in pH or  $c^\infty$ : these variations

are accompanied by swelling or shrinking of the particles, thereby influencing their size, i.e., their overall volume charge (ligand) density, and the inner charge (ligand) distribution within the shell. The theory reported in this study provides the basic elements for tackling such complex coupling between particle geometry, interphasial diffuseness, EDL electrostatics, and metal speciation dynamics in soft colloidal ligand suspensions. Metal speciation dynamics in suspensions of more involved biological systems such as bacteria or reactive biofilms, require refined consideration of, e.g., interphasial M and/or ML internalization and/or excretion mechanisms, the implementation of which along the lines discussed here being possible. The analysis has also pointed out that the course of bulk metal depletion (insets Figure 2) is necessarily coupled to the physicochemical (in particular electrostatic) determinants that govern the metal binding within the shell. Doing so, we foresee that relationships may be formulated between the dynamic speciation parameters of interest (in particular  $k_a^*$  and  $K^*$ ) and the rate of bulk metal depletion, which is accessible by the experiment. This will be the subject of a forthcoming analysis where the impact

of particle volume fraction on speciation dynamics will be further analyzed in details.

### List of Main Symbols and Abbreviations

$a$	radius of the core of the soft colloidal ligand particle (m)
$c_{i=M,ML}$	local concentration of species $i$ ( $=M, ML$ ) within a unit cell ( $\text{mol m}^{-3}$ )
$c_L^*$	bulk concentration of reactive sites within the soft part (shell layer) of the colloidal ligand particle ( $\text{mol m}^{-3}$ )
$c_M^*$	initial bulk concentration of free metal species ( $\text{mol m}^{-3}$ ) in the electrolytic solution
$c_p$	particle number concentration in the sample volume ( $\text{m}^{-3}$ )
$c^\infty$	bulk concentration of $z:z$ background electrolyte
$d$	thickness of the soft layer of the colloidal ligand particle (m)
$D_M$	diffusion coefficient of free metal within/outside the particle shell when its water content is sufficiently high ( $\text{m}^2 \text{s}^{-1}$ )
$D_{\text{particle}}$	diffusion coefficient of the particle ( $\text{m}^2 \text{s}^{-1}$ )
$f(r)$	radial function defined by eqs 4 and 5
$K^*$	stability constant for (ML) colloidal complex ( $\text{mol}^{-1} \text{m}^3$ )
$K$	chemical contribution to the stability constant for (ML) colloidal complex ( $\text{mol}^{-1} \text{m}^3$ )
$k_a$	association rate constant of the complex (ML) ( $\text{mol}^{-1} \text{m}^3 \text{s}^{-1}$ ) ( $k_a = K_{os} k_w$ )
$k_a^*$	effective association rate constant of the colloidal complex (ML)
$k_d$	dissociation rate constant of the complex (ML) ( $\text{s}^{-1}$ )
$k_d^*$	effective dissociation rate constant of the colloidal complex (ML)
$k_w$	rate constant for water substitution ( $\text{s}^{-1}$ )
$K_{os}$	stability constant of outer-sphere complex ( $\text{mol}^{-1} \text{m}^3$ )
$L$	ligand species
$l$	typical separation distance between neighboring reactive sites within the surface layer of the soft colloidal ligand particle
$M$	free metal species
$ML$	complex species
$r$	radial position (m)
$r_c$	characteristic dimension that enters the definition of the radius of a unit cell (m)
$t$	time (s)
$V_c$	volume of a unit cell ( $\text{m}^3$ )
$V_s$	volume of the shell layer component of the colloidal ligand particle ( $\text{m}^3$ )
$y(r)$	local dimensionless EDL electrostatic potential
$z_{i=M,L}$	valence of species $i = M, L$

### Greek Symbols

$\alpha$	decay length of the ligand distribution within the shell layer
$\phi$	volume fraction of soft colloidal ligand particles in the sample volume
$\psi$	local electrostatic potential at the interface soft particle/electrolyte solution
$\kappa$	reciprocal screening Debye layer thickness in the electrolytic medium
$\kappa_m$	reciprocal screening Debye layer thickness within the shell
$\mu_M$	electrochemical potential of free metal species $M$

$\rho_i^V$	volume concentration of species $i$ over the spatial region of a unit cell ( $\text{mol m}^{-3}$ )
$\rho_i^S$	volume concentration of species $i$ over the shell layer of the colloidal ligand particle ( $\text{mol m}^{-3}$ )
$\rho_i^{\text{el}}(r)$	local volume charge density within the surface layer of the soft colloidal ligand particle
$\rho_{\text{ions}}^{\text{el}}(r)$	local volume charge density stemming from the (mobile) ions present in the electrolytic medium

**Supporting Information Available:** Detailed steps for (i) the derivation of the time dependence for the effective colloidal complex association rate  $k_a^*$ , (ii) the derivation of the colloidal complex stability constant  $K^*$ , and (iii) the numerical analysis followed for evaluating the  $M$  and  $ML$  concentration profiles (and thus  $k_a^*$ ) as a function of time. Also included is the demonstration that Boltzmann statistics for  $M$  originates from the exact balance between  $M$  diffusion and migration transport across the interphase between particle and outer electrolytic medium. This information is available free of charge via the Internet at <http://pubs.acs.org>.

### References and Notes

- (1) Buffle, J. *Complexation reactions in aquatic systems. An analytical approach*; Ellis Horwood: Chichester, 1988.
- (2) Mota, A. M.; Correia, S. In *Metal speciation and Bioavailability*; Tessier, A., Turner, D., Eds.; John Wiley and Sons: New York, 1995; Chapter 5.
- (3) Florence, T. M.; Morrison, G. M.; Stauber, J. L. *Sci. Total Environ.* **1992**, 125, 1.
- (4) Van Leeuwen, H. P.; Town, R. M. *Environ. Sci. Technol.* **2003**, 37, 3945.
- (5) Capodaglio, G.; Scarponi, G.; Toscano, G.; Barbante, C.; Cescon, P. *Fresenius' J. Anal. Chem.* **1995**, 351 (4–5), 386.
- (6) Pinheiro, J. P.; Minor, M.; Van Leeuwen, H. P. *J. Electroanal. Chem.* **2006**, 587, 284.
- (7) Van Leeuwen, H. P.; Galceran, J. In *Physicochemical Kinetics and Transport at Biointerfaces*; Van Leeuwen, H. P., Koster, W., Eds.; John Wiley and Sons: Chichester, U.K., 2004; Chapter 4.
- (8) Wilkinson, K. J.; Buffle, J. In *Physicochemical Kinetics and Transport at Biointerfaces*; Van Leeuwen, H. P., Koster, W., Eds.; John Wiley and Sons: Chichester, U.K., 2004; Chapter 10.
- (9) Pinheiro, J. P.; Galceran, J.; Van Leeuwen, H. P. *Environ. Sci. Technol.* **2004**, 38, 2397.
- (10) Galceran, J.; Puy, J.; Salvador, J.; Cecilia, J.; Van Leeuwen, H. P. *J. Electroanal. Chem.* **2001**, 505, 85.
- (11) Galceran, J.; Puy, J.; Salvador, J.; Cecilia, J.; Mas, F.; Garces, J. L. *Phys. Chem. Chem. Phys.* **2003**, 5, 5091.
- (12) Davison, W. J. *Electroanal. Chem.* **1978**, 87, 395.
- (13) Pinheiro, J. P.; Mota, A. M.; van Leeuwen, H. P. *Colloids Surf. A* **1999**, 151, 181.
- (14) Pinheiro, J. P.; Minor, M.; Van Leeuwen, H. P. *Langmuir* **2005**, 21, 8635.
- (15) Botelho, C. M. S.; Boaventura, R. A. R.; Goncalves, M. L. S. S. *Anal. Chim. Acta* **2002**, 426, 73.
- (16) Botelho, C. M. S.; Boaventura, R. A. R.; Goncalves, M. L. S. S. *Electroanalysis* **2002**, 14, 1713.
- (17) Duval, J. F. L.; Pinheiro, J. P.; Van Leeuwen, H. P. *J. Phys. Chem. A* **2008**, 112, 7137.
- (18) Duval, J. F. L. Electrophoresis of soft colloids: basic principles and applications. In *Environmental Colloids and Particles: Behaviour, Separation and Characterization*; Wilkinson, K. J., Lead, J., Eds.; John Wiley and Sons: Chichester, U.K., 2007; Chapter 7.
- (19) Rotureau, E.; Thomas, F.; Duval, J. F. L. *Langmuir* **2007**, 23, 8460.
- (20) Duval, J. F. L.; Busscher, H. J.; Van de Belt-Gritter, B.; Van der Mei, H. C.; Norde, W. *Langmuir* **2005**, 21, 11268.
- (21) Duval, J. F. L.; Wilkinson, K. J.; van Leeuwen, H. P.; Buffle, J. *Environ. Sci. Technol.* **2005**, 39, 6435.
- (22) Langlet, J.; Gaboriaud, F.; Gantzer, C.; Duval, J. F. L. *Biophys. J.* **2008**, 94, 3293.
- (23) Gaboriaud, F.; Gee, M. L.; Strugnell, R.; Duval, J. F. L. *Langmuir* **2008**, 24, 10988.
- (24) Duval, J. F. L.; Ohshima, H. *Langmuir* **2006**, 22, 3533.
- (25) Zhang, Z.; Buffle, J.; Alemani, D. *Environ. Sci. Technol.* **2007**, 41, 7621.
- (26) Mason, T. G.; Lin, M. Y. *Phys. Rev. E* **2005**, 71, 040801.

- (27) Fernandez-Nieves, A.; de las Nieves, F. J.; Fernandez-Barbero, A. *J. Chem. Phys.* **2004**, *120*, 374.
- (28) Karim, A.; Satija, S. K.; Douglas, J. F.; Ankner, J. F.; Fetters, L. J. *Phys. Rev. Lett.* **1994**, *73*, 3407.
- (29) Glidle, A.; Swann, M. J.; Gadegaard, N.; Cooper, J. M. *J. Phys. B: Condens. Matter* **2000**, 276–278, 359.
- (30) Tran, Y.; Sanjuan, S.; Pantoustier, N.; Perrin, P. *Annual Scientific Report; Laboratoire Leon Brillouin*, 2005–2006; <http://www-llb.cea.fr>.
- (31) Muller, F.; Romet-Lemonne, G.; Delsanti, M.; Mays, J. W.; Daillant, J.; Guenoun, P. *J. Phys.: Condens. Matter* **2005**, *17*, S3355.
- (32) Doi, M.; Matsumoto, M.; Hirose, Y. *Macromolecules* **1992**, *25*, 5504.
- (33) Sierra-Martin, B.; Romero-Cano, M. S.; Cosgrove, T.; Vincent, B.; Fernandez-Barbero, A. *Colloids Surf. A* **2005**, 270–271, 296.
- (34) Hellweg, T.; Kratz, K.; Pouget, S.; Eimer, W. *Colloids Surf. A* **2002**, *202*, 223.
- (35) Zhou, F.; Hu, H.; Yu, B.; Osborne, V. L.; Huck, W. T. S.; Liu, W. *Anal. Chem.* **2007**, *79*, 176.
- (36) Rotureau, E.; Van Leeuwen, H. P. *J. Phys. Chem. A* **2008**, *112*, 7177.
- (37) Derek, M. *Biophys. J.* **2004**, *86*, 2630.
- (38) Scheutjens, J. M. H. M.; Fleer, G. J. *J. Phys. Chem.* **1979**, *83*, 1619.
- (39) Van Male, J. Self-consistent-field theory for chain molecules: extensions, computational aspects, and applications. Ph.D. thesis. Wageningen University, The Netherlands, 2003.
- (40) Lopez-Garcia, J. J.; Grosse, C.; Horno, J. *J. Colloidal Interface Sci.* **2003**, *265*, 341.
- (41) Lyklema, J. *Electric double layers. Fundamentals of Colloid and Interface Science*; Academic Press: New York, 1995; Chapter 3, Vol. 2.
- (42) Morel, F. M. M.; Hering, J. G. *Principles and applications of aquatic chemistry*; John Wiley: New York, 1993.
- (43) Eigen, M. *Z. Phys. Chem.* **1954**, *1*, 176.
- (44) Fuoss, R. *J. Am. Chem. Soc.* **1958**, *80*, 5059.
- (45) Van Leeuwen, H. P.; Town, R. M.; Buffle, J. *J. Phys. Chem. A* **2007**, *111*, 2115.
- (46) van Leeuwen, H. P. *Langmuir* **2008**, *24*, 11718.
- (47) Zhang, Z.; Buffle, J.; Startchev, K.; Alemani, D. *Environ. Chem.* **2008**, *5* (3), 204.
- (48) Stulik, K.; Amatore, C.; Holub, K.; Marecek, V.; Kutner, W. *Pure Appl. Chem.* **2000**, *72*, 1483.
- (49) Buffle, J.; Horvai, G. In *In situ monitoring of aquatic systems: chemical analysis and speciation*; Buffle, J., Horvai, G., Eds.; John Wiley and Sons: New York, 2000; pp 11–12.
- (50) Oldham, K. B. In *Microelectrodes: theory and applications*; Montenegro, M. I.; Queiros, M. A.; Daschbach, J. L., Eds.; Kluwer: Dordrecht, The Netherlands, 1991; p 35.
- (51) Bard, A. J.; Faulkner, L. In *Electrochemical methods: fundamentals and applications*; John Wiley and Sons: New York, 2001.
- (52) Duval, J. F. L. *Langmuir* **2005**, *21*, 3247.
- (53) Ohshima, H. *J. Colloid Interface Sci.* **2008**, *323*, 92.
- (54) Duval, J. F. L.; Van Leeuwen, H. P. *Langmuir* **2004**, *20*, 10324.

JP809764H



# SUPPORTING INFORMATION

## Metal speciation dynamics in soft colloidal ligand suspensions. Electrostatic and site distribution aspects.

Jérôme F.L. Duval

Laboratory Environment and Mineral Processing, Nancy-University, CNRS  
UMR CNRS-INPL 7569, BP 40 – F-54501 Vandoeuvre-lès-Nancy Cedex, France.

### 1. Boltzmann statistics, a balance between diffusion and migration transports.

In the equilibrium chemical regime, the derivatives of the local M and ML concentrations with respect to time vanish so that summing eqs 13 and 14 leads to

$$a \leq r \leq a+d: \quad D_M \nabla_r^2 c_M^e(r) + \frac{z_M D_M}{z} \left\{ \frac{\partial c_M^e(r)}{\partial r} \frac{\partial y(r)}{\partial r} + c_M^e(r) \nabla_r^2 y(r) \right\} = 0, \quad (S1)$$

where the superscript ‘e’ holds for quantities at equilibrium. It is immediately seen that the above equation is also valid for radial positions  $a \leq r \leq a+r_c$  (eq 15) under the condition  $\partial c_M(r, t) / \partial t = 0$ . Equation S1 may then be rewritten in the form

$$a \leq r \leq a+r_c: \quad \frac{1}{r^2} \frac{\partial}{\partial r} \left( r^2 \frac{\partial c_M^e(r)}{\partial r} \right) = - \frac{z_M}{z} \nabla \cdot \left\{ c_M^e(r) \frac{\partial y(r)}{\partial r} \right\} \quad (S2)$$

with  $\nabla \cdot G(r) \equiv \frac{1}{r^2} \frac{\partial}{\partial r} (r^2 G(r))$  the divergence operator applied to a radial function  $G$ . After straightforward simplification and integration of eq S2 between  $a$  and  $r$ , we obtain

$$a \leq r \leq a+r_c: \quad \frac{\partial c_M^e(r)}{\partial r} = - \frac{z_M}{z} c_M^e(r) \frac{\partial y(r)}{\partial r}. \quad (S3)$$

Second integration provides

$$a \leq r \leq a+r_c: \quad c_M^e(r) = c_M^e(r = a + r_c) \exp \left\{ z_M [y(r = a + r_c) - y(r)] / z \right\}, \quad (S4)$$

which is the well-known Boltzmann statistic distribution for M species across the interphase between particle and outer electrolytic medium.

### 2. Derivation of the effective kinetic rate constants $k_a^*$ and $k_d^*$ .

The integration of eq 13 for  $i=ML$  over the shell volume leads to

$$\frac{\partial \rho_{ML}^s(t)}{\partial t} = -k_d \rho_{ML}^s(t) + \frac{4\pi c_L^*}{V_s} k_a \int_a^{a+d} r^2 c_M(r, t) f(r) dr, \quad (S5)$$

where we have introduced the ML concentration  $\rho_{\text{ML}}^{\text{s}}$  over the shell layer volume of the particle:

$$\rho_{\text{ML}}^{\text{s}}(t) = \frac{4\pi}{V_{\text{s}}} \int_a^{a+d} r^2 c_{\text{ML}}(r, t) dr, \quad (\text{S6})$$

with  $V_{\text{s}} = 4\pi \left\{ (a+d)^3 - a^3 \right\} / 3$  the volume over which the reactive binding sites L are distributed.

The condition of conservation of total binding sites throughout the soft diffuse interphase when changing  $\alpha/d$  and/or  $d$  is ensured by eq 5. This allows us to write

$$\rho_{\text{L}}^{\text{V}} / c_{\text{L}}^* = V_{\text{s}} / V_{\text{c}}. \quad (\text{S7})$$

Substitution of eq S7 into eq S5 and multiplication of both sides of the resulting equation by  $V_{\text{s}} / V_{\text{c}}$  yields

$$\frac{\partial \rho_{\text{ML}}^{\text{V}}(t)}{\partial t} = -k_{\text{d}} \rho_{\text{ML}}^{\text{V}}(t) + k_{\text{a}} \rho_{\text{L}}^{\text{V}} \rho_{\text{M}}^{\text{s}}(t), \quad (\text{S8})$$

where we have used the relationship  $\rho_{\text{ML}}^{\text{V}}(t) / \rho_{\text{ML}}^{\text{s}}(t) = V_{\text{s}} / V_{\text{c}}$  (obtained from combining eq 28 for  $i=\text{ML}$  with eq S6) and we have defined the concentration  $\rho_{\text{M}}^{\text{s}}$  over the shell volume by

$$\rho_{\text{M}}^{\text{s}}(t) = \frac{4\pi}{V_{\text{s}}} \int_a^{a+d} r^2 c_{\text{M}}(r, t) f(r) dr. \quad (\text{S9})$$

Let introduce the colloidal complex stability constant  $K^*$  defined by

$$K^* = k_{\text{a}}^* / k_{\text{d}}^*. \quad (\text{S10})$$

Then, eliminating the time-derivative terms between eqs 27 and S8 and using eq S10, one obtains the searched general relationship (eq 30 in the main text) between  $k_{\text{a}}^*$  and  $k_{\text{a}}$ :

$$\frac{k_{\text{a}}^*(t)}{k_{\text{a}}} = \frac{\rho_{\text{M}}^{\text{s}}(t) \rho_{\text{L}}^{\text{V}} - \rho_{\text{ML}}^{\text{V}}(t) K^{-1}}{\rho_{\text{M}}^{\text{V}}(t) \rho_{\text{L}}^{\text{V}} - \rho_{\text{ML}}^{\text{V}}(t) K^{*-1}}, \quad (\text{S11})$$

where the time-dependences of  $\rho_{\text{M}}^{\text{s}}$ ,  $\rho_{\text{M}}^{\text{V}}$ ,  $\rho_{\text{ML}}^{\text{V}}$  and  $k_{\text{a}}^*$  have been written explicitly. The remaining issue is the derivation of the expression for the stability constant  $K^*$ , which is presented below.

Under chemical equilibrium conditions reached at  $t \rightarrow \infty$  where  $\partial \rho_{\text{ML}}^{\text{V}}(t) / \partial t = 0$ , eq S8 shows that

$$\frac{k_{\text{a}}}{k_{\text{d}}} = \frac{\rho_{\text{ML}}^{\text{V,e}}}{\rho_{\text{L}}^{\text{V}} \rho_{\text{M}}^{\text{s,e}}}, \quad (\text{S12})$$

where the superscript ‘e’ refers to quantities defined at chemical equilibrium. Similarly, eq 27 provides at  $t \rightarrow \infty$

$$\frac{k_a^*}{k_d^*} = \frac{\rho_{ML}^{V,e}}{\rho_L^V \rho_M^{V,e}}. \quad (S13)$$

Recalling that the intrinsic (chemical) stability constant of ML complex is given by  $K = k_a / k_d$ , the combination of eqs S10, S12 and S13 gives

$$K^* = K \frac{\rho_M^{s,e}}{\rho_M^{V,e}} \quad (S14)$$

Equations 13-15 may be straightforwardly integrated under chemical equilibrium conditions ( $\partial \rho_{i=M,ML}^V(t) / \partial t = 0$ ), and the results reads as the well-known Boltzmann formulation, *i.e.* eq S4.

As shown above, eq S4 basically results from the balance between free metal migration and diffusion fluxes. For cases where  $\kappa r_c \gg 1$ , *i.e.* in the absence of EDL overlap between adjacent particles, eq S4 reduces to

$$c_M^e(r) = c_M^e(r = a + r_c) \exp(-z_M y(r) / z). \quad (S15)$$

Combining eqs S9, S14 and S15, we finally obtain

$$\frac{K^*}{K} = \frac{V_c}{V_s} \frac{\int_a^{a+d} r^2 f(r) \exp(-z_M y(r) / z) dr}{\int_a^{a+r_c} r^2 \exp(-z_M y(r) / z) dr}, \quad (S16)$$

which is eq 32 in the main text.

### 3. Numerical analysis for evaluating the M and ML concentration profiles.

In this section, the numerical analysis of eqs 13-22 is detailed for the case where there is no significant overlap between electric double layers (EDL) around adjacent particles (*i.e.*  $\kappa r_c \gg 1$ ). From a numerical point of view, this situation is the most complex since the associated partial differential equations (eqs 13-15) are stiff with EDL extensions ( $\kappa^{-1} \sim O(1\text{nm} - 30\text{nm})$  for  $c^\infty = 0.1\text{mM} - 100\text{mM}$ ) that are several orders of magnitude shorter than the free metal diffusion length scale at steady-state ( $O(\mu\text{m})$ ).

For the sake of mathematical and numerical convenience, we introduce the dimensionless variables

$$\tilde{t} = t D_M / \left[ p(a+d)^2 \right], \quad (S17)$$

$$k_{an} = k_a p(a+d)^2 c_L^* / D_M, \quad (S18)$$

$$k_{\text{dn}} = k_{\text{d}} p (a + d)^2 / D_{\text{M}}, \quad (\text{S19})$$

$$x = (r - a) / (a + d), \quad (\text{S20})$$

$$\text{and} \quad \tilde{c}_{\text{M,ML}}(r, t) = c_{\text{M,ML}}(r, t) / c_{\text{M}}^*. \quad (\text{S21})$$

One of the difficulties in the original formulation of the problem as given in [17] is the existence of a sharp discontinuity at the radial position  $r = a + d$  that marks the transition between the reactive particle phase and the electrolyte medium. This difficulty is here circumvented by the introduction of the continuous function  $f$  given by eqs 4-5. The continuity of  $f$  is verified for any position  $r \in [a, a + r_{\text{c}}]$  and any values of  $\alpha / d$ . The set of eqs 13-15 may then be reduced to

$$a \leq r \leq a + r_{\text{c}} : \begin{cases} \frac{\partial \tilde{c}_{\text{ML}}(x, \tilde{t})}{\partial t} = -\{k_{\text{dn}} \tilde{c}_{\text{ML}}(x, \tilde{t}) - k_{\text{an}} c_{\text{M}}(x, \tilde{t}) f(x)\} \\ \frac{\partial \tilde{c}_{\text{M}}(x, \tilde{t})}{\partial t} = p \nabla_x^2 \tilde{c}_{\text{M}}(x, \tilde{t}) + \{k_{\text{dn}} c_{\text{ML}}(x, \tilde{t}) - k_{\text{an}} c_{\text{M}}(x, \tilde{t}) f(x)\} \\ + p \frac{z_{\text{M}}}{z} \left\{ \frac{\partial c_{\text{M}}(x, \tilde{t})}{\partial x} \frac{\partial y(x)}{\partial x} + c_{\text{M}}(x, \tilde{t}) \nabla_x^2 y(x) \right\} \end{cases} \quad (\text{S22, S23})$$

with  $\nabla_x^2 \equiv \frac{\partial^2}{\partial x^2} + \frac{2}{x + a / (a + d)} \frac{\partial}{\partial x}$ . The dimensionless time  $\tilde{t}$  is discretized according to

$$k = 1, \dots, N : \quad \tilde{t}_k = (k - 1) \Delta t, \quad (\text{S24})$$

with  $N$  an integer and  $\Delta t = 1 / (N - 1)$  the time discretization step. Replacing the time derivatives in eqs S22, S23 by their implicit backward Euler finite element differences equivalent, we obtain

$$a \leq r \leq a + r_{\text{c}} :$$

$$\begin{cases} \tilde{c}_{\text{ML}}^{k+1}(x) = -\{k_{\text{dn}} \tilde{c}_{\text{ML}}^{k+1}(x) - k_{\text{an}} \tilde{c}_{\text{M}}^{k+1}(x) f(x)\} \Delta t + \tilde{c}_{\text{ML}}^k(x) \\ \tilde{c}_{\text{M}}^{k+1}(x) = p \Delta t \nabla_x^2 \tilde{c}_{\text{M}}^{k+1}(x) + \{k_{\text{dn}} \tilde{c}_{\text{ML}}^{k+1}(x) - k_{\text{an}} \tilde{c}_{\text{M}}^{k+1}(x) f(x)\} \Delta t \\ + p \Delta t \frac{z_{\text{M}}}{z} \left\{ \frac{\partial \tilde{c}_{\text{M}}^{k+1}(x)}{\partial x} \frac{\partial y(x)}{\partial x} + \tilde{c}_{\text{M}}^{k+1}(x) \nabla_x^2 y(x) \right\} + \tilde{c}_{\text{M}}^k(x) \end{cases} \quad (\text{S25, S26})$$

, where we define  $\tilde{c}_{\text{M,ML}}^k(x) = \tilde{c}_{\text{M,ML}}(x, \tilde{t}_k)$ . Let us now pose  $Y_1^{k+1}(x) = \tilde{c}_{\text{M}}^{k+1}(x)$  and  $Y_2^{k+1}(x) = \partial \tilde{c}_{\text{M}}^{k+1}(x) / \partial x$ . Combining eqs S25-S26, one shows that eq S26 may be rearranged in a set of two ordinary differential equations of the first order as follows



$a \leq r \leq a + r_c :$

$$\begin{cases} \frac{dY_1^{k+1}(x)}{dx} = Y_2^{k+1}(x) \\ \frac{dY_2^{k+1}(x)}{dx} = -Y_2^{k+1}(x) \left\{ \frac{2}{x+a/(a+d)} + \frac{z_M}{z} \frac{\partial y(x)}{\partial x} \right\} + Y_1^{k+1}(x) \left[ \frac{1}{p\Delta t} + \frac{k_{an}}{p} f(x) - \right. \\ \left. \frac{z_M}{z} \nabla_x^2 y(x) - \frac{1}{p} \frac{k_{dn} k_{an} \Delta t f(x)}{1 + k_{dn} \Delta t} \right] - \Omega^k(x) \end{cases} \quad (S27, S28)$$

, with 
$$\Omega^k(x) = \frac{1}{p\Delta t} Y_1^k(x) + \frac{1}{p} \frac{k_{dn}}{1 + k_{dn} \Delta t} \tilde{c}_{ML}^k(x) \quad (S29)$$

Let  $\mathfrak{S}$  be a numerical solver which enables the calculation of the searched  $Y_1^{k+1}(x)$  and  $Y_2^{k+1}(x)$  at any  $k$  for a given function  $\Omega^k$ , *i.e.*

$$k = 1, \dots, N-1: \quad Y_{1,2}^{k+1}(x) = \mathfrak{S}(\Omega^k(x)). \quad (S30)$$

The function  $\Omega^1$  corresponds to the situation at  $\tilde{t} = 0$  with  $Y_1^1(x) (= \tilde{c}_M^1(x))$  and  $\tilde{c}_{ML}^1(x)$  provided by eqs 16-18. Iterating  $k$  from 1 to  $N-1$ , eq S30 leads to the evaluation of  $Y_1^{k+1}(x)$  and  $Y_2^{k+1}(x)$ , recalling that the local concentrations  $\tilde{c}_{ML}^{k+1}(x)$  and  $\tilde{c}_{ML}^k(x)$  are interrelated *via* the recursive relationship S25 which reads as

$$a \leq r \leq a + r_c: \quad \tilde{c}_{ML}^{k+1}(x) = (1 + k_{dn} \Delta t)^{-1} \left\{ k_{an} \Delta t Y_1^{k+1}(x) f(x) + \tilde{c}_{ML}^k(x) \right\}. \quad (S31)$$

Equations S27-S31 thus provide the M and ML concentrations profiles at any time  $\tilde{t}_k$ . Let us now describe the numerical procedure subsumed in the solver  $\mathfrak{S}$ .

The set of differential equations (S27-S28) may be written for a given  $\tilde{t}_k$  in the concise form

$$i = 1, 2: \quad \frac{dY_i^{k+1}(x)}{dx} = \Gamma_i(x, Y_1^{k+1}, Y_2^{k+1}), \quad (S32)$$

with  $(\Gamma_i)_{i=1,2}$  the operators that define the right hand sides of eqs S27 ( $i=1$ ) and S28 ( $i=2$ ). At

$x = x_1 = 0$ ,  $Y_2^{k+1}$  satisfies eq 19 rewritten as

$$Y_2^{k+1}(x_1) = 0. \quad (S33)$$

At the position  $x_1$ , we set

$$Y_1^{k+1}(x_1) = \zeta_I^{k+1}, \quad (S34)$$

where  $\zeta_1^{k+1}$  is a time-dependent parameter to be subsequently determined. At the edge of the unit cell, *i.e.* at the position  $x = x_2 = r_c / (a + d)$ , eq 20 provides

$$Y_2^{k+1}(x_2) = 0, \quad (\text{S35})$$

and we define  $Y_1^{k+1}(x_2)$  as

$$Y_1^{k+1}(x_2) = \zeta_2^{k+1}, \quad (\text{S36})$$

with  $\zeta_2^{k+1}$  a second time-dependent variable to be evaluated. The two boundary problem (S32)-(S36) is solved by numerical shooting from the position  $x_1$  to  $x_f$  (forward shooting, denoted as FS) and from the position  $x_2$  to  $x_f$  (backward shooting, denoted as BS) with  $x_1 < x_f < x_2$  and

$$Y_1^{k+1}(x_f)_{\text{BS}} = Y_1^{k+1}(x_f)_{\text{FS}}, \quad (\text{S37})$$

$$Y_2^{k+1}(x_f)_{\text{BS}} = Y_2^{k+1}(x_f)_{\text{FS}}. \quad (\text{S38})$$

For that purpose,  $\zeta_1^{k+1}$  and  $\zeta_2^{k+1}$  are iteratively updated with a globally convergent Newton-Raphson<sup>1</sup> scheme till the continuity equations S37 and S38 are satisfied. This method called ‘shooting to a fitting point’ (located at  $x = x_f$ ) is based on the use of an adaptive stepsize Runge-Kutta method of the fifth-order implemented with the aforementioned Newton-Raphson scheme.<sup>1</sup> Within this procedure, many small steps tiptoe through treacherous spatial regions (especially at the edge of the shell layer *i.e.* at  $x = d / (a + d)$ ) where strong variations of the function to be determined are encountered, while larger step sizes are automatically defined in ‘uninteresting spatial zones’ where smooth function gradients are computed (*i.e.* far from the shell layer). Doing so, fast convergence is met for  $x_f \sim d / (a + d)$ .

Following the above numerical strategy, the author verified that two modes of computations are equivalent. In the first mode, the resolution of the time dependent M and ML concentration profiles is carried out according to eq S30 with initial guesses for  $\zeta_1^{k+1}$  and  $\zeta_2^{k+1}$  obtained from the solutions at  $\tilde{t}_k$ . In the second mode, the computation is performed according to

$$Y_{1,2}^{k+1}(x) = \Im(\Omega^1(x)), \quad (\text{S39})$$

where the time  $\tilde{t}_k$  (eq S24) is now iterated upon changing  $N$  on the premise that  $\Delta t = 1 / (N - 1)$  remains well below 1.

The accuracy and stability of the numerical solution was systematically verified by controlling the independence of the results on the quantities  $x_f$ ,  $p$ ,  $\Delta t$ , the initial guesses for  $\zeta_1^{k+1}$  and  $\zeta_2^{k+1}$  as

well as the convergence criterion that defines how well the continuity conditions S37-S38 for  $Y_{1,2}^{k+1}$  at  $x = x_f$  are satisfied. Typical values for  $N$  around 300 or above lead to numerical results with accuracy up to three digits.

Once the spatial and temporal dependences of  $c_{M,ML}$  are known and therewith the EDL potential distribution throughout the soft interphase (see point 4 below), the calculation of the quantities  $K^*$ ,  $\rho_M^S(t)$ ,  $\rho_M^V(t)$  and  $\rho_{ML}^V(t)$  may be easily carried out *via* the numerical evaluations (using Simpson's rule<sup>1</sup>) of the various integrals involved in eqs 28, S9 and 32. Following this, eq 30 straightforwardly leads to the searched ratio  $k_a^*(t)/k_a$ .

The evaluation of the time- and space-dependent M and ML concentration profiles as previously described requires knowledge of the scaled equilibrium potential  $y$ . Derivation of the latter is presented below.

#### 4. Numerical analysis for evaluating the equilibrium potential profile.

The spatial variable  $r$  is now rewritten in dimensionless form as follows

$$\tilde{x} = (r - a) / R_o, \quad (S40)$$

and is discretised according to

$$i = 1, \dots, M : \quad \tilde{x}_i = (i - 1) \Delta \tilde{x}, \quad (S41)$$

with  $\Delta \tilde{x} = 1 / (M - 1)$  the space discretization step and  $R_o$  the position where  $dy/d\tilde{x}|_{\tilde{x}=1} < \varepsilon$  with  $\varepsilon$  a prescribed scalar satisfying  $\varepsilon \ll 1$ , typically of the order of  $10^{-4}$  or lower. It is recalled that  $R_o \ll r_c$  for  $\kappa r_c \gg 1$ . Given eqs S40-S41, the finite element differences formulation of eqs 7, 23-26 is given by

$$i = 2, \dots, M - 1 : \quad y_{i+1} - 2y_i \left[ 1 - \frac{\Delta \tilde{x}}{\tilde{x}_i + a / R_o} \right] + y_{i-1} \left[ 1 - \frac{2\Delta \tilde{x}}{\tilde{x}_i + a / R_o} \right] - (\kappa R_o \Delta \tilde{x})^2 \left\{ \sinh(y_i) - \frac{z_L c_L^*}{2z c_\infty} f(\tilde{x}_i) \right\} = 0 \quad (S42)$$

$$y_2 - y_1 = 0 \quad (S43)$$

$$y_M - y_{M-1} = 0 \quad (S44)$$

, with  $y_i = y(\tilde{x}_i)$ . The non-linear tridiagonal system that consists of the  $M$  equations (S42-S44) with the  $(y_i)_{i=1, \dots, M}$  as unknown variables, was solved using a globally convergent Newton-Raphson method already invoked above.  $R_o$  was iteratively updated till the far field condition (S44)-

equivalent to setting  $y(\tilde{x}=1)=0$  under the condition  $\kappa r_c \gg 1$  - was satisfied within the predefined convergence criterion  $dy/d\tilde{x}|_{\tilde{x}=1} < \varepsilon$ . Initial guesses for  $R_o$  and  $(y_i)_{i=1,\dots,M}$  were obtained from the analytical solution of the linearized Poisson-Boltzmann equation (Debye-Hückel approximation) given by eq 34. It was systematically verified that the computed potential distributions were independent of the electrostatic cut-off condition  $dy/d\tilde{x}|_{\tilde{x}=1} < \varepsilon$  and on the grid size ( $M \sim 400$  or larger). Once the electric potential distribution is known on the uniform grid  $(\tilde{x}_i)_{i=1,\dots,M}$ , it is cubic-spline interpolated in the  $r$ -space region  $[a, a+r_c]$  (with  $y(r > a+R_o)=0$  and  $dy(r)/dr|_{r>a+R_o}=0$ ) or equivalently in the  $x$ -space region  $[0, r_c/(a+d)]$  as defined by eq S20. Subsequently, the Laplacian term  $\nabla_x^2 y$  appearing in eq S28 may be evaluated for any position  $x$  according to the expression

$$\nabla_x^2 y(x) = [\kappa(a+d)]^2 \left\{ \sinh[y(x)] - \frac{z_L c_L^*}{2zc^\infty} f(x) \right\}, \quad (\text{S45})$$

which directly follows from eqs 7, 12, 23 and 24. The electric field  $dy(x)/dx$  involved in eq S28 may be straightforwardly estimated *via*

$$\frac{dy(x)}{dx} = \frac{a+d}{R_o} \frac{dy(\tilde{x})}{d\tilde{x}}, \quad (\text{S46})$$

where  $dy(\tilde{x})/d\tilde{x}$  is the function cubic-spline interpolated from the field values  $(y_{i+1} - y_i)_{i=1,\dots,M-1} / \Delta\tilde{x}$  evaluated on the uniform grid  $(\tilde{x}_i)_{i=1,\dots,M}$ . The author experienced that this way of determining the double layer electric field, while very accurate for  $\kappa d \gg 1$ , suffers at  $\kappa d = O(1)$  from instability at spatial positions located in the vicinity of  $r = a + d$ , *i.e.* in the EDL region where the potential distribution is the steepest. This instability is reflected in subtle but significant (a few percent) variations of  $dy(\tilde{x})/d\tilde{x}|_{\tilde{x} \sim d/R_o}$  upon variation of  $R_o$  and/or  $M$  even for  $\Delta\tilde{x}$  values as low as  $< 10^{-3}$ . This feature ultimately leads to very inaccurate evaluation of  $k_a^*/k_a$  at low  $\kappa d$ , thereby recalling that the coupled electric field and M/ML concentration gradients exhibit abrupt developments in the vicinity of  $r = a + d$ . To solve for this issue, the electric field was determined as follows. Posing  $Y^{(1)}(x) = dy/dx$  (with  $x$  defined by eq S20), one may show on the basis of the non-linear PB equation (eqs 23-24) that the electric field  $Y^{(1)}$  is governed by



$$\frac{dY^{(1)}(x)}{dx} = -\frac{2}{x + a/(a+d)}Y^{(1)}(x) + \nabla_x^2 y(x) \quad (\text{S47})$$

where  $\nabla_x^2 y(x)$  is yielded by eq S45. Equation S47 is solved following a numerical procedure of the type ‘shooting to a fitting point’ similar to that employed for solving eqs S32-S36. For that purpose, the boundaries verified by  $Y^{(1)}$  at  $x = x_1 = 0$  and  $x = x_2 = r_c/(a+d)$  (eqs 25-26 in the main text) are written in the form

$$Y^{(1)}(x_1) = \nu_1 \quad (\text{S48})$$

and 
$$Y^{(1)}(x_2) = 0, \quad (\text{S49})$$

with  $\nu_1$  a scalar to be determined. The advantage of this method over that which consists in evaluating the electric field on the basis of a uniform grid, is the use of an adaptive step size-mesh with, in particular, detailed computation in the vicinity of  $x = d/(a+d)$  ( $\sim x_f$ ). The value of  $\nu_1$  is updated by means of a globally convergent Newton Raphson method till continuity of the electric field is met at  $x = x_f$ . Comparison of eqs S48 with eq 25 reveals that  $\nu_1$  must be zero, in agreement with the numerical outcome (typical values obtained for  $\nu_1$  are well below  $10^{-4}$ ). The consistency of the above method for evaluating the field distribution was verified by changing the starting guess value chosen for  $\nu_1$  as well as the convergence criterion that defines how well the continuity condition for the electric field at  $x = x_f$  is met. Finally, the electric field was cubic-spline interpolated over the whole  $x$ -space region  $[0, r_c/(a+d)]$  on the basis of the field values obtained on the non-uniform mesh grid. The resulting function, which allows the evaluation of the electric field for any position  $x$ , was then employed within the numerical scheme adopted for solving the M and ML concentration profiles.

## References.

[1] Press, W. H.; Teukolsky, S. A.; Vetterling, W. T.; Flannery, B. P. in *Numerical recipes in Fortran, The Art of Scientific Computing*, 2<sup>nd</sup> ed.; Cambridge University Press: New-York, 1986.